Near- infrared spectroscopic observations of high redshift C-I absorbers

Zou, S.; Petitjean, P.; Noterdaeme, P.; Ledoux, C.; Krogager, J. -K.; Fathivavsari, H.; Srianand, R.; Lopez, S.

Astronomy & Astrophysics

Near-infrared spectroscopic observations of high redshift C I absorbers[*],[**]

S. Zou[1], P. Petitjean[1], P. Noterdaeme[1], C. Ledoux[2], J.-K. Krogager[1,6], H. Fathivavsari[3],
R. Srianand[4], and S. López[5]

[1] Sorbonne Université, CNRS, UMR 7095, Institut d'Astrophysique de Paris, 98 Bis Bd Arago, 75014 Paris, France
e-mail: zou@iap.fr
[2] European Southern Observatory, Alonso de Córdova 3107, Casilla 19001, Vitacura, Santiago, Chile
[3] School of Astronomy, Institute for Research in Fundamental Sciences (IPM), PO Box 19395-5531, Tehran, Iran
[4] Inter-University Center for Astronomy and Astrophysics, Post Bag 4, Ganeshkhind, 411 007, Pune, India
[5] Departamento de Astronomía, Universidad de Chile, Casilla 36-D, Santiago, Chile
[6] Dark Cosmology Centre, Niels Bohr Institute, Copenhagen University, Juliane Maries Vej 30, 2100 Copenhagen Ø, Denmark

ABSTRACT

We study a sample of 17 $z > 1.5$ absorbers selected based on the presence of strong C I absorption lines in Sloan Digital Sky Survey (SDSS) spectra and observed with the European Southern Observatory Very Large Telescope (ESO-VLT) spectrograph X-shooter. We derive metallicities, depletion onto dust, and extinction by dust, and analyse the absorption from Mg II, Mg I, Ca II, and Na I that are redshifted into the near infrared wavelength range. We show that most of these C I absorbers have high metallicity and dust content. We detect nine Ca II absorptions with $W(\text{Ca II}\lambda3934) > 0.23$ Å out of 14 systems where we have appropriate wavelength coverage. The observed equivalent widths are similar to what has been measured in other lower redshift surveys of Ca II systems. We detect ten Na I absorptions in the 11 systems where we could observe this absorption. The median equivalent width ($W(\text{Na I}\lambda5891) = 0.68$ Å) is larger than what is observed in local clouds with similar H I column densities but also in $z < 0.7$ Ca II systems detected in the SDSS. The systematic presence of Na I absorption in these C I systems strongly suggests that the gas is neutral and cold, maybe part of the diffuse molecular gas in the interstellar medium of high-redshift galaxies. Most of the systems (12 out of 17) have $W(\text{Mg II}\lambda2796) > 2.5$ Å and six of them have log $N(\text{H I}) < 20.3$, with the extreme case of J1341+1852 that has log $N(\text{H I}) = 18.18$. The Mg II absorptions are spread over more than $\Delta v \sim 400$ km s^{-1} for half of the systems; three absorbers have $\Delta v > 500$ km s^{-1}. The kinematics are strongly perturbed for most of these systems, which indicates that these systems probably do not arise in quiet disks and must be close to regions with intense star-formation activity and/or are part of interacting objects. All this suggests that a large fraction of the cold gas at high redshift arises in disturbed environments.

Key words. infrared: galaxies – methods: observational – techniques: spectroscopic – Galaxy: abundances – galaxies: kinematics and dynamics

1. Introduction

Damped Lyman-α systems (DLA) observed in the spectra of bright background sources are produced by neutral gas (Wolfe & Prochaska 2000) located in the halo and/or disk of galaxies. The gas in DLAs at high redshift consists mostly of a warm neutral phase (e.g. Petitjean et al. 2000b), with average temperatures of the order of several thousand kelvin. Most high-z DLAs are found to have low metallicities ($\sim$0.1 solar, Srianand et al. 2012; Rafelski et al. 2014) and the cosmological density of the gas in DLAs is much less than the cosmological density of stars (Noterdaeme et al. 2012a). All this is in line with the idea that most DLAs are part of a transition phase intermediate between the intergalactic medium, which is the reservoir of

gas for galaxy formation, and the dense and cold gas that is an ingredient for star formation in the disks of galaxies.

Understanding the mechanisms of star formation at high redshifts is central to our knowledge of how galaxies formed and subsequently evolved chemically. Stars form in molecular clouds (e.g. Snow & McCall 2006) that are located in the interstellar medium (ISM) of galaxies whose properties are regulated in turn by radiative and mechanical feedback from stars. Deriving the physical properties of the gas in the ISM, in particular in the diffuse molecular phase of galaxies, is crucial for our understanding of how stars formed in the early Universe. It is not easy to detect the cold neutral as in absorption and attempts to do so have been made for many years. In particular, attention has been brought to molecular hydrogen as it has numerous detectable absorption lines in the ultraviolet (UV; Ledoux et al. 2003; Cui et al. 2005; Noterdaeme et al. 2008). It has been shown that H$_2$ is detected with overall molecular fractions >0.1% in about 10% of the DLAs (Noterdaeme et al. 2008) or possibly less (Jorgenson et al. 2014). When detected, the associated gas is usually cold with $T_e \sim 150$ K and dense with $n_H \sim 100$ cm^{-3} (Srianand et al. 2005; Balashev et al. 2011). The latter systems directly trace the diffuse ISM of high-redshift galaxies and are places where it

---

is possible to study the relation between the physical properties of the ISM and star-formation activity (Noterdaeme et al. 2012b). These are also places where one can probe the H I-to-H$_2$ transition in the diffuse interstellar medium of high-redshift galaxies (Noterdaeme et al. 2015; Ma et al. 2015; Balashev et al. 2017).

It is not that easy to preselect systems where molecular hydrogen can be found. One way is to concentrate on the presence of neutral carbon. Indeed, carbon can be ionized by photons of energy smaller than the H I ionization limit and its detection should indicate the presence of neutral, cold, and well-shielded gas, thus the presence of H$_2$. Neutral-carbon (C I) at high redshift has not been searched for systematically so far (see however Ge & Bechtold 1997, 1999; Srianand et al. 2005). We have thus embarked in a survey of systems selected only on the basis of the presence of strong C I absorption in quasar spectra from the Sloan Digital Sky Survey (SDSS). The selection of systems, the main characteristics of the sample, the detection rate, and the H I content have been described in Ledoux et al. (2015) and the detailed analysis of the metallicities will be discussed in Ledoux et al. (in prep). Out of 66 strong C I systems detected in the SDSS DR7, 17 have been observed with the ESO spectrograph X-shooter, which offers the unique opportunity to study the associated metal lines redshifted in the infrared region of the spectrum and in particular the Ca II, Na I, and Ti II lines that are frequently used in the local universe to study the interstellar medium. The large spectral range of X-shooter is also ideal for deriving the dust attenuation of the quasar spectrum induced by the presence of a DLA along the line of sight. One of these systems has been singled out as a "ghostly" DLA and is described in details in Fathivavsari et al. (2017).

The presence of Ca II absorption is of particular interest for studying the properties of the interstellar medium of high-z galaxies. It is important to bear in mind that Ca is usually highly depleted onto dust and that the ionization energy of Ca II being 11.87 eV, Ca II may not be the dominant ionization stage of Ca even in H I dominated gas. Even though the presence of strong Ca II absorption is therefore not a characteristic of cold gas, its presence or absence can yield interesting information on the amount of dust and on the radiation density below the Lyman limit. In turn, Na I is ionized above 5.14 eV and is therefore associated with cold and neutral gas. In the local universe a tight correlation is seen between N(Na I) and N(H I) (Ferlet et al. 1985; Wakker & Mathis 2000). It will be interesting to verify if such correlation holds at high redshift as well. In addition the ratio of the Na I and Ca II column densities is a useful indicator of the physical state of the gas (Routly & Spitzer 1952; Welty et al. 1996).

In our Galaxy, when observed at high spectral resolution, the Na I complexes break into sub-components with a median Doppler parameter of $\sim$0.73 km s^{-1} and a median separation between adjacent components of $\sim$2 km s^{-1}. The typical temperature of the gas is 80 K (Welty et al. 1994). The velocity distribution of the corresponding Ca II absorption is broader, due to outlying components at higher temperature ($T > 6000$ K) seen only in Ca II. Even individual Ca II components are broader than the corresponding Na I or K I components implying that the Ca II absorption arises predominantly in warmer and more diffuse gas occupying a larger volume (Hobbs 1974, 1975; Welty et al. 1996; Welty & Hobbs 2001). Absorption of Ca II can arise both from cold, relatively dense gas, where Ca is typically heavily depleted onto grains and Ca II is its dominant ionization state, and also in warmer, lower density gas, where Ca is less depleted but Ca II is a trace ionization state.

It is found that Ca II(Na I) absorbers at intermediate and high radial velocities are present in 40–55% (20–35%) of the sightlines through the halo of our Galaxy (Bekhti et al. 2008; Ben Bekhti et al. 2012). The Ca II/Na I ratio is found to be smaller in halo gas compared to what is observed in the disk of the Galaxy (Keenan et al. 1983; Ferlet et al. 1985; Vladilo et al. 1993; Sembach et al. 1993; Ben Bekhti et al. 2012).

Previous studies of Ca II and Na I absorption outside the Galaxy were carried out at low redshift so that the absorption lines are redshifted in the optical window (see Blades et al. 1988; Bowen et al. 1991). The impact parameters of the Ca II-associated galaxies have also been studied previously (Kunth & Bergeron 1984; Womble et al. 1990; Petitjean et al. 2000a; Hall et al. 2002; Wang et al. 2005; Cherinka & Schulte-Ladbeck 2011; Zych et al. 2007; Rahmani et al. 2016).

Wild & Hewett (2005) were the first to search SDSS spectra systematically for Ca II absorbers and to show that they induce a reddening of the quasar spectrum with an average $E(B - V) = 0.06$ (Wild et al. 2006) and that they are more evolved than the overall population of DLAs. Sardane et al. (2014, 2015) used SDSS-data release 9 data and showed that the equivalent width distribution reveals two populations of Ca II systems with W_r(Mg IIλ2796)/W_r(Ca IIλ3934) less and greater than 1.8, respectively. These authors show as well that the systems with W_r(Ca IIλ3934) smaller and larger than $\sim$0.7 Å have properties, respectively, consistent with those of halo gas and intermediate between halo-type and disk-type gas (see Zych et al. 2009). Guber & Richter (2016) study the dust depletion of Ca II and Ti II in 34 systems at $z < 0.4$ and conclude that these lines trace predominantly neutral gas in the disks and inner halo regions of galaxies (see also Cox et al. 2007). Finally, Na I and Ca II have been detected in a DLA at $z \sim 1$ towards QSO APM 08279+5255 (Petitjean et al. 2000a). In this system, it is clear that Na I absorption is confined to narrow components whereas Ca II has a shallow and broad profile very much consist with what have been found in the Galaxy and its halo.

The paper is organised as follows. We describe the sample and the observations in Sect. 2. Section 3 gives the Na I, Ca II, and $E(B - V)$ measurements. We discuss the results in Sect. 4 before concluding in Sect. 5.

2. Sample and observations

We systematically searched the SDSS-DR7 (Abazajian et al. 2009) quasar spectra (Schneider et al. 2010) for C I absorption systems and found 66 of them at $z > 1.5$ with W_r(C Iλ1560) > 0.12 Å. The sample is complete for W_r(C Iλ1560) > 0.40 Å (Ledoux et al. 2015). Follow-up observations have been performed with the ESO Ultraviolet and Visual Echelle Spectrograph (UVES) spectrograph for 27 systems and the ESO/X-shooter spectrograph for 17 systems (see Ledoux et al., in prep). In this paper we concentrate on the latter systems.

The instrument X-shooter (Vernet et al. 2011) covers the full wavelength range from 300 nm to 2.5 μm at intermediate spectral resolution using three spectroscopic arms (UV-blue (UVB), visible (VIS) and near-IR (NIR)). We observed the quasars in slit mode for slightly more than one hour each. To optimise the sky subtraction in the NIR, telescope nodding was performed following an ABBA scheme with a nod throw of 5 arcsec and a jitter box of 1 arcsec. The two-dimensional (2D) and one-dimensional (1D) spectra were extracted using the X-shooter pipeline in its version 2.5.2 (Modigliani et al. 2010).

Table 1. Column density measurements using Voigt profile fitting.

QSO	z_{abs}	log N(H I)	log N(Fe II)	log N(Zn II)	log N(Si II)	[Fe/Zn]	[Fe/H][c]	[Si/H][c]	[Zn/H][c]
J0216−0021	1.7359	20.01 ± 0.04	14.41 ± 0.05	–	15.21 ± 0.09	–	-1.10 ± 0.07	-0.31 ± 0.10	–
J0815+2640	1.6798	20.78 ± 0.04	14.89 ± 0.05	13.36 ± 0.08	15.52 ± 0.07	-1.41 ± 0.09	-1.39 ± 0.07	-0.77 ± 0.07	0.02 ± 0.08
J0854+0317	1.5663	20.46 ± 0.06	14.96 ± 0.11	12.97 ± 0.12	15.58 ± 0.11	-0.95 ± 0.16	-1.00 ± 0.12	-0.39 ± 0.12	-0.05 ± 0.13
J0917+0154	2.1059	20.75 ± 0.04	15.44 ± 0.11	13.64 ± 0.05	16.17 ± 0.06	-1.14 ± 0.12	-0.97 ± 0.12	-0.25 ± 0.08	0.17 ± 0.07
J1047+2057	1.7740	20.48 ± 0.04	15.04 ± 0.17	13.12 ± 0.11	15.68 ± 0.08	-1.02 ± 0.20	-0.94 ± 0.18	-0.31 ± 0.09	0.08 ± 0.12
J1122+1437	1.5538	20.33 ± 0.04	13.87 ± 0.05	12.26 ± 0.24	14.72 ± 0.09	-1.33 ± 0.25	-1.96 ± 0.08	-1.12 ± 0.10	-0.63 ± 0.25
J1133−0057	1.7045	21.00 ± 0.32^a	14.23 ± 0.03	13.16 ± 0.06	15.71 ± 0.06	-1.87 ± 0.07	-2.27 ± 0.32	-0.80 ± 0.33	-0.40 ± 0.33
	1.7063								
J1237+0647	2.6896	19.89 ± 0.48	14.53 ± 0.06	–	15.26 ± 0.22	–	-1.01 ± 0.49	-0.29 ± 0.53	–
J1248+2848	1.5124	–	15.07 ± 0.17	12.82 ± 0.19	15.75 ± 0.06	-0.69 ± 0.25	–	–	–
J1302+2111	1.6556	21.27 ± 0.28	15.45 ± 0.16	13.15 ± 0.09	16.01 ± 0.05	-0.64 ± 0.18	-1.32 ± 0.32	-0.77 ± 0.29	-0.68 ± 0.30
J1314+0543	1.5829	19.97 ± 0.04	14.52 ± 0.10	12.98 ± 0.15	15.36 ± 0.11	-1.40 ± 0.18	-0.95 ± 0.11	-0.12 ± 0.12	0.45 ± 0.16
J1341+1852	1.5442	18.18 ± 0.07	12.98 ± 0.05	–	13.92 ± 0.11	–	^{b}	^{b}	–
J1346+0644	1.5120	–	14.70 ± 0.07	13.15 ± 0.08	15.51 ± 0.08	-1.39 ± 0.11	–	–	–
J2229+1414	1.5854	19.51 ± 0.12	14.38 ± 0.05	12.09 ± 0.19	15.29 ± 0.12	-0.65 ± 0.20	-0.63 ± 0.14	0.27 ± 0.17	0.02 ± 0.23
J2336−1058	1.8287	20.30 ± 0.06	14.98 ± 0.06	13.15 ± 0.13	15.54 ± 0.07	-1.11 ± 0.14	-0.86 ± 0.09	-0.31 ± 0.09	0.25 ± 0.15
J2340−0053	2.0546	20.26 ± 0.11	14.96 ± 0.06	12.62 ± 0.08	15.14 ± 0.08	-0.60 ± 0.10	-0.81 ± 0.13	-0.64 ± 0.14	-0.21 ± 0.14
J2350−0052	2.4265	20.45 ± 0.05	14.79 ± 0.03	12.89 ± 0.06	15.36 ± 0.05	-1.04 ± 0.07	-1.17 ± 0.07	-0.61 ± 0.08	-0.13 ± 0.08

[a] Value from the fit by Fathivavsari et al. (2017). [b] Ionization correction should be taken into account. [c] We added the molecular contribution to the total hydrogen column density whenever H_2 is detected (see Noterdaeme et al. 2018).

Table 2. Equivalent widths (Å) of absorption features.

| QSO	C Iλ1560	C Iλ1656	Na Iλ5891	Na Iλ5897	Ca IIλ3934	Ca IIλ3969	Mg IIλ2798	Mg IIλ2803	Mg Iλ2852
J0216−0021	0.32 ± 0.14	0.84 ± 0.11	0.34 ± 0.05	0.09 ± 0.03	0.23 ± 0.09	<0.22	2.62 ± 0.04	2.21 ± 0.05	0.78 ± 0.04
J0815+2640	0.63 ± 0.14	0.99 ± 0.13	0.82 ± 0.21	0.45 ± 0.14	0.47 ± 0.16	<0.31	2.89 ± 0.06	2.69 ± 0.05	–
J0854+0317	0.26 ± 0.07	0.46 ± 0.08	<0.23	<0.23	0.66 ± 0.28	<0.12	2.89 ± 0.04	2.73 ± 0.03	0.79 ± 0.06
J0917+0154	0.36 ± 0.10	0.61 ± 0.32	–	–	<0.53	<0.53	3.81 ± 0.09	3.73 ± 0.08	1.59 ± 0.11
J1047+2057	0.77 ± 0.17	1.17 ± 0.13	0.86 ± 0.15	0.75 ± 0.14	0.59 ± 0.14	0.50 ± 0.15	3.50 ± 0.06	3.68 ± 0.04	1.33 ± 0.05
J1122+1437	0.19 ± 0.09	0.26 ± 0.08	0.56 ± 0.10	0.53 ± 0.09	0.21 ± 0.24	<0.28	0.83 ± 0.03	0.65 ± 0.03	0.21 ± 0.03
J1133−0057	0.85 ± 0.17	1.42 ± 0.17	1.00	0.88	0.17 ± 0.07	0.07 ± 0.10	2.91 ± 0.07	2.80 ± 0.09	1.20 ± 0.06
	–	–	0.88	0.67	–	–	–	–	–
J1237+0647	0.39 ± 0.22	0.60 ± 0.17	0.51 ± 0.21	0.34 ± 0.23	–	<0.16	4.28 ± 0.16	3.84 ± 0.21	0.99 ± 0.24
J1248+2848	0.35 ± 0.13	0.55 ± 0.17	–	–	0.87 ± 0.10	0.75 ± 0.20	4.03 ± 0.07	3.68 ± 0.07	1.21 ± 0.10
J1302+2111	0.51 ± 0.19	0.59 ± 0.17	0.80 ± 0.21	<0.40	1.06 ± 0.30	0.48 ± 0.20	2.87 ± 0.07	2.73 ± 0.06	1.30 ± 0.09
J1314+0543	0.46 ± 0.13	0.65 ± 0.15	0.92 ± 0.13	1.00 ± 0.12	<0.35	<0.35	2.04 ± 0.08	1.79 ± 0.09	0.43 ± 0.08
J1341+1852	0.13 ± 0.06	0.14 ± 0.06	–	–	<0.14	<0.14	0.32 ± 0.01	0.25 ± 0.02	0.03 ± 0.01
J1346+0644	0.50 ± 0.19	0.80 ± 0.18	–	–	<0.31	<0.31	2.98 ± 0.07	2.69 ± 0.07	0.84 ± 0.11
J2229+1414	0.15 ± 0.22	0.21 ± 0.24	0.51 ± 0.14	0.37 ± 0.12	<0.50	<0.50	2.70 ± 0.13	2.32 ± 0.11	0.51 ± 0.11
J2336−1058	0.25 ± 0.09	0.35 ± 0.06	0.24 ± 0.11	0.17 ± 0.07	–	–	3.08 ± 0.05	2.68 ± 0.04	1.23 ± 0.07
J2340−0053	0.11 ± 0.02	0.17 ± 0.03	–	–	0.25 ± 0.02	0.10 ± 0.10	1.66 ± 0.01	1.53 ± 0.01	0.47 ± 0.01
J2350−0052	0.32 ± 0.08	0.51 ± 0.03	–	–	–	–	3.06 ± 0.05	2.66 ± 0.05	0.80 ± 0.08

Generally the final spectra are close to the nominal resolving power of $R = 4350$, 7450, and 5300 in the UVB, VIS, and NIR arms, for slit widths of 1.0, 0.9, and 0.9 arcsec, respectively. For some objects however, the seeing was better than the widths of the slits, and resolutions were higher. We estimated the actual resolution following the method described in Fynbo et al. (2011). Flux calibration has been performed using observations of standard stars provided by the ESO. We note that observations have been performed when the Atmospheric Dispersion Corrector (ADC) was still in use.

There is no clear distinction between the X-shooter subsample and the overall sample of C I absorbers. A comparison between sub-samples will be performed in Ledoux et al. (in prep). Names of the objects and characteristics of the C I absorption systems derived from X-shooter data are given in Tables 1 and 2. Spectra and absorption profiles are shown in the Appendices.

3. Measurements

3.1. Equivalent widths

For isolated transitions we measure the equivalent width (EW) directly from the spectrum, integrating the observed normalized flux over the absorption profile. In the case of C I, the C I, C I*, and C I** transitions are blended together so that we used the program VPFIT (Carswell & Webb 2014) to disentangle the absorptions. Results of the fits are shown in Appendix A. Equivalent widths of the overall C I $\lambda\lambda$1560,1656 absorption with errors measured at the 1σ level are given in Cols. 2 and 3 of Table 2. These values are derived by integrating the observed normalized flux in the spectrum, except for QSO J0917+0154; in this case, C Iλ1560 is strongly blended with other metal lines, thus we used the value obtained from the fit. We follow Vollmann & Eversberg (2006) to estimate the errors.
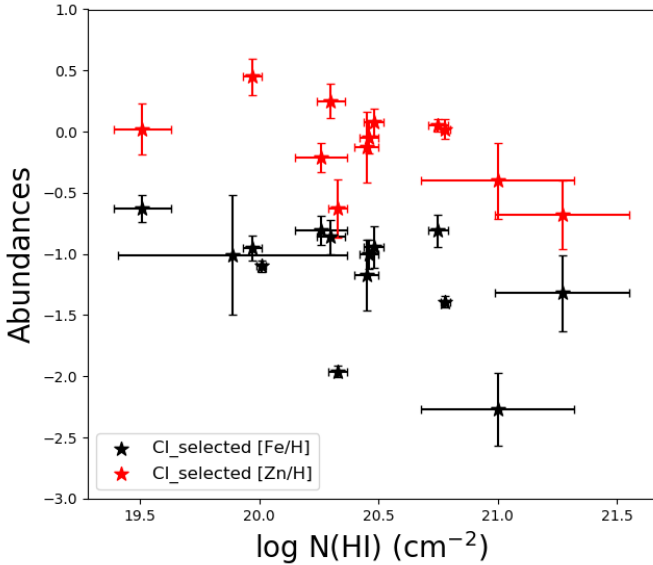
Fig. 1. Metal abundances versus $N(\text{H I})$ column density in our sample, red stars are for [Zn/H] and black stars are for [Fe/H]. We use the gasphase metal abundances and H I column densities from Table 1.

Fig. 2. *Left panel*: depletion factor [Zn/Fe] versus W(C Iλ1560). *Right panel*: depletion factor [Zn/Fe] versus metallicity, [Zn/H]. The purple dashed line in the *right panel* is the mean relation observed for typical DLAs (Berg et al. 2015).

When Na I and/or Ca II absorption lines are detected, we fit the absorption feature with a Gaussian function and derive the equivalent widths from the fit. The results are shown in Appendix A. When no line is detected, we derive an upper limit on the equivalent width as $EW_{\text{lim}} = 3.2 \times FWHM/SNR$ in 3σ where SNR is the signal-to-noise ratio (S/N) at the expected position of the line, and full width at half maximum ($FWHM$) corresponds to twice the width of an unresolved spectral feature. The absorption redshift is determined by the position of the strongest C I component and is used as the zero of the velocity scale for the figures in Appendix A.

3.2. Metallicities and extinction

The spectral resolution of X-shooter is not high enough to obtain trustful Doppler parameters and column densities except when either the absorption is optically thin (e.g. Zn II) or several transitions of the same species are observed. This is the case for Fe II and Si II for which we derive column densities from Voigt profile fitting of all observed transitions together (see Table 1). We used VPFIT (Carswell & Webb 2014) to model the absorption profiles. The redshift and Doppler parameter of the components were imposed to be the same in all profiles. When estimating best-fit parameters, VPFIT takes as input the normalised spectrum and the resolution provided by the user. This means that continuum placement uncertainties are not reflected in the error estimates. We therefore estimated the errors in column densities by varying slightly the continuum for lines that are not fully saturated. When one of the lines was optically thin, we derived the error in the column density from the error in the equivalent width (see Sect. 3.1). For other species we measured only the equivalent width without trying to derive a column density.

Gas-phase metal abundances derived from Fe II, Si II, and Zn II absorptions are listed in Table 1. We added the molecular contribution to the total hydrogen column density whenever H$_2$ was detected (see Noterdaeme et al. 2018). This contribution is non-negligible in the cases of J1237+0647 and J0917+0154. We plot in Fig. 1 the metal abundances versus H I column density
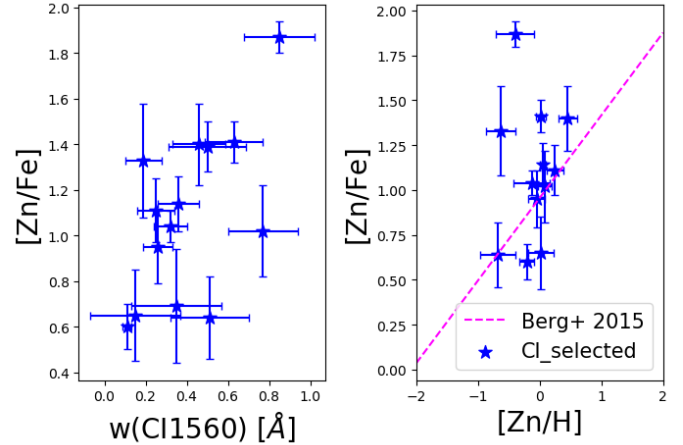
(red and black stars for, respectively, Zn and Fe). It is apparent that the C I systems have large metallicities (around solar) and in any case larger than what is measured in typical DLAs at similar redshifts (e.g. Rafelski et al. 2014). Depletion of iron onto dust measured as [Zn/Fe] is significant. What is striking also is that not only are H I column densities not very large (several systems do not qualify as standard DLAs as they show log $N(\text{H I}) < 20.3$), but also there is a tendency for metallicity to decrease as column density increases. This may well be a consequence of the usual dust bias, which implies that systems with both high H I column densities and metallicities drop out of the sample, because the quasar flux is attenuated below the flux limit of the quasar survey (Boissé 1995). It could be as well that the quasars colours are affected by the presence of dust, shifting the quasar out of colour selection of the quasar survey.

The dust depletion indicator [Zn/Fe] is plotted versus $W(\text{C I}\lambda1560)$ and metallicity (as [Zn/H]) in the two panels of Fig. 2. It is apparent in the left panel that dust depletion is significant. There is, however, no strong correlation between the amount of dust depletion and the amount of neutral carbon. The relation seems to hold even for the high metallicities measured in our sample although a large scatter is observed in the measured depletion factors. Although these considerations are useful for the following discussion, it is clear that these properties should be studied in the complete sample of C I systems, not only in the sub-sample of quasars observed with X-shooter. This will be done in a companion paper (Ledoux et al. in prep).

Given the metallicities and dust depletions measured in our sample, the quasar spectra are significantly attenuated by the presence of dust in the absorption systems. We estimate this attenuation, measured as A_V and $E(B-V)$, by fitting a quasar spectral template to the data assuming a set of fixed extinction curves (Small Magellanic Cloud (SMC), Large Magellanic Cloud (LMC), and LMC2) parametrized by Gordon et al. (2003). The dust reddening is assumed to be caused solely by the foreground C I absorber. We use the quasar template derived by Selsing et al. (2016) and fit only the data in bona fide continuum regions, regions which are not strongly affected by absorption or broad emission lines. This template has been obtained by combining seven spectra of bright quasars taken with X-shooter. Signal-to-noise ratio varies from 50 in the UV to 200 in the optical and 100 in the near infrared. Before fitting, the template is smoothed with

Table 3. Dust extinction in the sample

QSO	Ext law	$E(B-V)$	A(V)	Rv	UVB S/N	VIS S/N	NIR S/N
J0216−0021	LMC2	0.123	0.34	2.76	49	66	55
J0815+2640	LMC	0.138	0.47	3.41	35	39	18
J0854+0317	SMC	0.099	0.27	2.74	52	66	50
J0917+0154	SMC	0.135	0.37	2.74	22	25	8
J1047+2057	LMC2	0.174	0.47	2.76	60	69	27
J1122+1437	N/A	0.000	0.00	2.74	35	76	35
J1133−0057	SMC	0.226	0.62	2.74	45	63	50
J1237+0647	LMC2	0.152	0.42	2.76	40	55	21
J1248+2848	N/A	0.000	0.00	2.74	28	33	28
J1302+2111	SMC	0.051	0.14	2.74	30	33	16
J1314+0543	SMC	0.036	0.10	2.74	42	45	20
J1341+1852	SMC	0.033	0.09	2.74	75	80	22
J1346+0644	N/A	0.018	0.05	2.74	29	32	30
J2229+1414	N/A	0.000	0.00	2.74	25	28	11
J2336−1058	N/A	0.007	0.02	2.74	62	65	40
J2340−0053	SMC	0.066	0.18	2.74	150	180	115
J2350−0052	LMC	0.038	0.13	3.41	50	70	35

The second column is the extinction law used when fitting the dust attenuation. The mean S/Ns in each of the X-shooter arms are given in the last three columns.
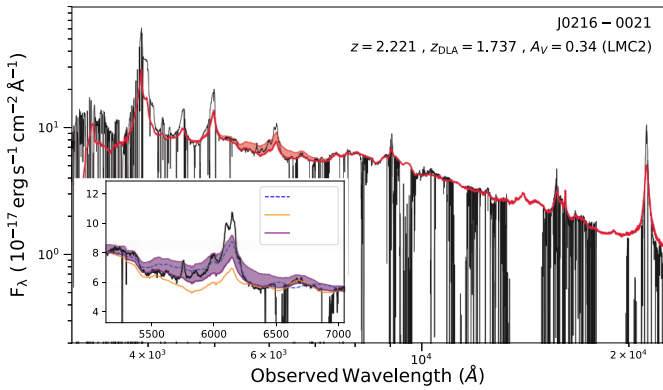
Fig. 3. X-shooter spectrum of J0216−0021. The red curve corresponds to the quasar template of Selsing et al. (2016) reddened by different extinction curves (see insert).

a Gaussian kernel ($\sigma = 7$ pixels) to prevent the noise in the template from falsely fitting noise peaks in the real data. In order to take into account the uncertainty in the template, we subsequently convolve the errors on the observed data with the uncertainty estimate for the template. In the near infrared, we perform a 5-σ clipping in order to discard outlying pixels introduced by the removal of skylines during data reduction. We furthermore allow for variations in the iron pseudo-continuum in the rest-frame UV by including the template derived by Vestergaard & Wilkes (2001). We separate the contributions from Fe II and Fe III into different templates and allow each to vary independently.

During the observations of the target J1302+2111, the atmospheric dispersion correction (ADC) malfunctioned leading to strong chromatic slit losses for the UVB and VIS arms (the NIR arm does not have an ADC unit and hence is not affected). Similar artefacts from malfunctioning ADCs of X-shooter have been reported by López et al. (2016). By comparing the X-shooter spectrum to the available SDSS spectrum, we conclude that the UVB arm is not strongly affected by chromatic slit loss, however, the VIS arm is heavily affected. We therefore do not use the VIS arm for the extinction analysis.

We then fit the template to the data using four free parameters: the attenuation A_V, the two scaling parameters for the Fe II and Fe III contributions, and an arbitrary flux scale that corresponds to the flux in the IR as the attenuation is usually negligible at these wavelengths. We fit the template to the data for each of the three extinction curves considered, SMC, LMC, and LMC2, and we assign the best fit as the solution with the lowest χ^2. We note that for the target J2340−0052, the lowest χ^2 is obtained with an LMC2 extinction law, however, upon visual inspection it is clear that the fit is not good as the best-fit iron contribution over-estimates the actual fluctuations in the data. Thus, when removing the iron contribution the spectrum is fitted better with the SMC extinction curve. The best-fit reddening and the associated best-fit extinction curve are given in Table 3. In cases where the reddening is too small to distinguish between various extinction curves, we list the best-fit extinction curve as "N/A" in Table 3 and give the R_V value for the SMC curve for simplicity. We note that for such small values of A_V, the value of R_V does not change the resulting $E(B-V)$ significantly. The main uncertainty for the dust fitting comes from intrinsic variations to the template. We have modelled this by assuming a distribution of the relative intrinsic spectral slope ($\Delta\beta$) as modelled by a Gaussian function with a width of 0.2 dex (Selsing et al. 2016). This yields an estimated 0.07 mag uncertainty on the best-fit A_V, which by far dominates the total uncertainty as the statistical uncertainty from the fit is of the order of 0.01 mag.

For the cases where an SMC extinction curve is preferred by the fit, the resulting A_V should be regarded as an upper limit, since for this extinction curve it is very difficult to disentangle dust in the quasar and dust in the absorber (see discussion in Krogager et al. 2015). In Fig. 3, we show the best-fit model for one target (the other spectra are shown in Appendix B).
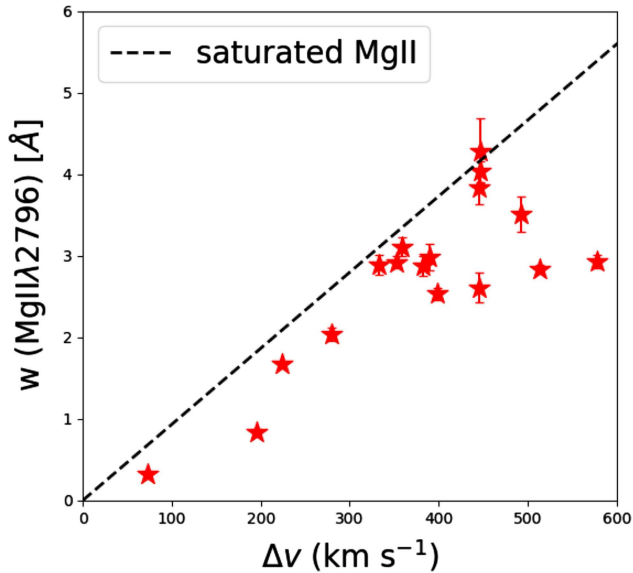
4. Results

4.1. MgII

The $W(\text{Mg II}\lambda2796)$ observed in our C I systems are large; 13 out of 17 (82%) of these systems have $W(\text{Mg II}\lambda2796) > 2.5$ Å, while
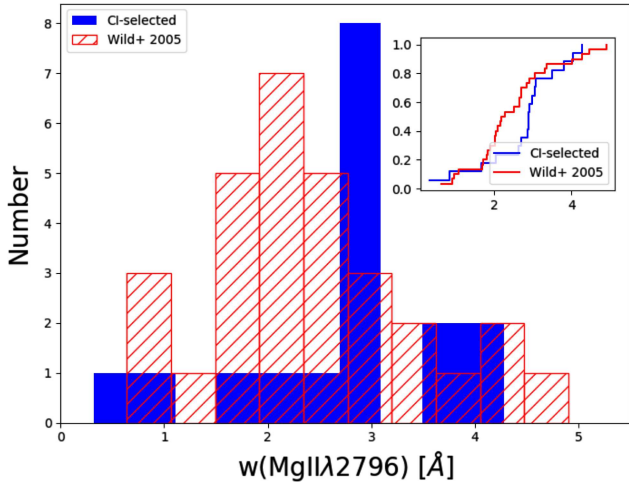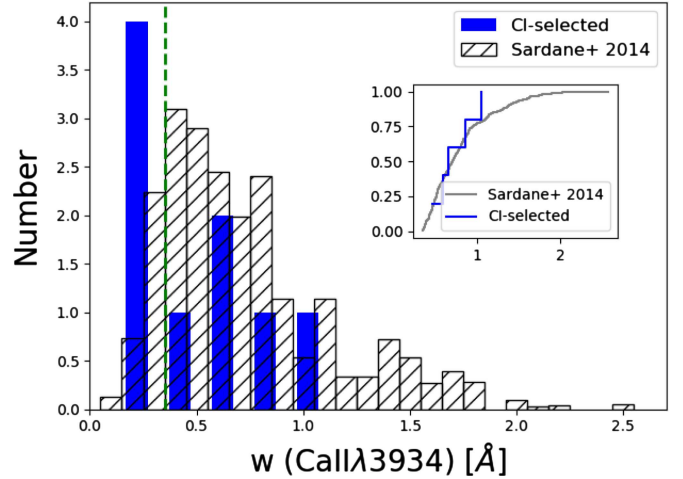
Fig. 4. W(Mg $\text{II}\lambda2796$) distributions. The blue histogram is for our sample of C I absorbers. The red hashed histogram is for the Ca II sample of Wild & Hewett (2005) at $0.84 < z < 1.3$. The lines in the insert are the cumulative distributions of the two samples.

Fig. 5. W(Mg $\text{II}\lambda2796$) versus the width of the absorption profile (see text for definition). The black dashed line is the relation expected when the Mg II line is totally saturated.

Fig. 6. Blue histogram is the rest equivalent width distribution of the Ca II K lines detected in our sample; grey-hashed histogram is the scaled equivalent width distribution of Ca II K lines detected in the SDSS by Sardane et al. (2014). The two cumulative distributions are shown in the insert; considering the detection limit of SDSS, we applied the Kolmogorov-Smirnov test when W(Ca $\text{II}\lambda3934$) > 0.35 Å.
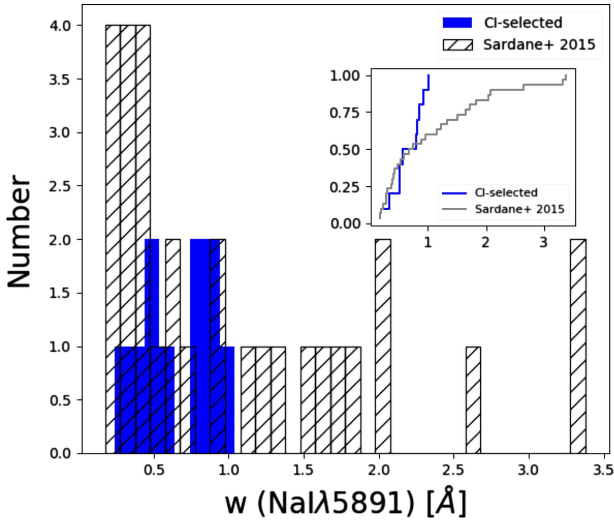
the absorption. In Fig. 5, it can be seen that the W(Mg $\text{II}\lambda2796$) equivalent width is strongly correlated with Δv. The correlation we see is quite similar to what is seen for typical DLAs (Ellison 2006). The difference resides again in the presence in our sample of a high fraction of large ($>300\,\text{km s}^{-1}$) Δv values. The median value of Δv in our sample is $\sim 400\,\text{km s}^{-1}$; three absorbers have $\Delta v > 500\,\text{km s}^{-1}$. Few such extreme systems are known in the literature at high redshift (Ledoux et al. 2006) and are found to be associated with molecular hydrogen (Petitjean et al. 2002; Ledoux et al. 2002). Only three DLAs out of 36 have a kinematical extention larger than $200\,\text{km s}^{-1}$ in the sample of Berg et al. (2016), when seven of our systems have $\Delta v > 400\,\text{km s}^{-1}$. It is therefore surprising that our CI-selected systems show such disturbed kinematics. The dashed line in Fig. 5 is the relation one expects if the lines are completely saturated over the whole absorption profile. It is therefore clear that above $300\,\text{km s}^{-1}$, the velocity spread of the absorption is dominated by satellite components.

These large kinematical spreads could be due to strong winds or the consequences of interactions between several galaxies. Interestingly, we found three systems in the spectra of J1047+2057, J1133−0057, and J2350−0052 where the Mg II absorption shows two distinct saturated sub-systems separated by more than $200\,\text{km s}^{-1}$ in the C I and Mg II absorption profiles. In J1133−0057, we detect also two distinct Na I components. Therefore probably both processes can be invoked to explain the large velocity spreads of Mg II absorptions in our sample.

4.2. Ca II

Due to the absorber redshifts, the Na I and Ca II lines in our sample are redshifted to the near-infrared wavelength range. The data quality in the NIR arm is not good enough to derive robust column densities. Thus we decided to use the equivalent width only to discuss the observations of Na I and Ca II. The results are listed in Table 2. We detect Ca II in nine systems out of 14 where we could obtain an equivalent width limit. The other spectra are spoiled by atmospheric features.

Wild & Hewett (2005) and Sardane et al. (2014) searched for Ca II systems in the SDSS data and therefore at $z_{\text{abs}} < 1.3$. Nestor et al. (2008) searched for Ca II in 16 known DLAs with

such strong systems are rare in Mg II surveys even at high redshifts (see Rao et al. 2005). As can be seen in Fig. 4, this is systematically larger than what is observed in systems selected on the basis of the presence of Ca II in SDSS spectra (Wild & Hewett 2005; red histogram in Fig. 4). The sample of Wild & Hewett (2005) includes 31 Ca II absorbing systems in the redshift range $0.84 < z < 1.3$. This number of strong systems can be compared with what is observed in high-redshift DLAs. Berg et al. (2016) study the 36 blindly selected DLAs with $2 < z < 4$ detected in the XQ-100 legacy survey (López et al. 2016). Only three of their DLAs have W(MgII$\lambda2696$) > 2.5 Å and much lower metallicities.

We have measured the velocity spread of the Mg II absorption, Δv. Since, the S/R in the infrared is not optimal, we measure Δv as the velocity separation between the two extreme pixels where $\tau < 0.1$. This is similar to the standard Δv_{90} definition and more robust for our data. The idea is to include all satellite absorption and to have a good representation of the kinematical extent of

Fig. 7. Blue histogram is the rest equivalent width distribution of the Na I lines detected in our sample; grey-hashed histogram is the equivalent width distribution of Na I lines detected in the SDSS by [Sardane et al. (2015)](#). The two cumulative distributions are shown in the insert.

$0.6 < z_{abs} < 1.3$ and detected Ca II in 12 of them. They warn, however, that their sample is biased towards strong Mg II systems. The Mg II mean equivalent width in their sample is 1.9 Å compared to 1.35 Å in an unbiased sample. The sample by Rahmani et al. (2016) consists of nine DLAs at $z \sim 0.6$. In five of the seven observed fields they could detect associated galaxies for which they estimate a metallicity of 0.2 to 0.9 solar when the gas has a metallicity in the range 0.05 to 0.6 solar.

Sardane et al. (2014) found 435 Ca II doublets in the SDSS DR7 and DR9 databases, with $z < 1.34$. In Fig. 6 we plot their equivalent width distribution (scaled for convenience and shown in black histograms) together with ours (blue histogram). There is no obvious difference between the two distributions. The discrepancy in the first bin is probably due to the higher detection limit of the SDSS study. Assuming the SDSS detection limit is ~ 0.35 Å, we applied a Kolmogorov-Smirnov test above this limit. A *p* value of 0.96 indicates that the two samples are drawn from a similar population.

4.3. Na I

We detect Na I in ten systems out of 11 systems for which the spectral range has a good S/N. In other spectra, the wavelength range where the Na I absorption is expected to be redshifted is spoiled by atmospheric features. Results are listed in Col. 4 of Table 2. We compare in Fig. 7 the Na I rest equivalent width distribution in our sample to the distribution in the sample of $30 z < 0.7$ Ca II systems detected in SDSS spectra by Sardane et al. (2015). It is apparent that the sample by Sardane et al. contains more systems with large Na I equivalent widths. We caution, however, that a few of these systems have inconsistent doublet ratios. We therefore checked the absorption in the SDSS spectra and noticed that some of the strong lines are affected by noise. A few strong Na I systems seem to be real, however. It seems that in the sample of C I-selected systems the strong Na I systems are missing. This is somewhat surprising as we would expect some correlation between Na I and C I absorptions (see Fig. 11). This possibly can be explained by the fact that strong Na I systems drop out of our sample because of additional extinction, as the corresponding extinction

does affect the spectrum more strongly at higher redshift. Alternatively there could be some evolution with redshift, strong Na I systems being absent at high redshift. This could be related to the possibility that strong winds are more frequent at lower redshift.

5. Properties of C I systems at high redshift

5.1. Dust dimming

Vladilo et al. (2006) studied the extinction induced by DLAs on the quasar flux. They found that the extinction A_V increases with the column density of iron locked into dust calculated as follows:

$$N(\text{Fe})_{\text{dust}} = N(\text{Fe}) - N(\text{Fe})_{\text{gas}}$$
$$= N(\text{Zn})_{\text{gas}} \times (10^{[\text{Fe}/\text{Zn}]_\odot} - 10^{[\text{Fe}/\text{Zn}]_{\text{gas}}}). \quad (1)$$

In Fig. 8 we plot the attenuation A_V versus the column density of iron into dust measured in the C I systems. Points by Vladilo et al. (2006) are indicated as blue triangles. Apart from a few points with low A_V, the trend is found to be the same for the different samples. We note that these low values are quite uncertain. We note also that most of our systems have log $N_{\text{dust}}(\text{Fe}) \sim 16$. It has been shown that for a column density larger than this, the molecular hydrogen content of DLAs is high (Ledoux et al. 2003; Noterdaeme et al. 2008). We calculated the dust-to-gas ratio κ_X based on the metallicity [X/H] and iron to metal ratio [Fe/X], according to the definition in Ledoux et al. (2003),

$$\kappa_X = 10^{[\text{X}/\text{H}]}(1 - 10^{[\text{Fe}/\text{X}]}). \quad (2)$$

It is clear that this ratio is directly proportional to the metallicity. We therefore plot this number minus the metallicity as a function of zinc metallicity in the right panel of Fig. 8. It can be seen this number is larger at higher metallicities (see also Wiseman et al. 2017). It is intriguing as well to see that the scatter is much less as soon as metallicity gets closer to the solar value. This may be a consequence of these systems being somehow chemically mature. Ledoux et al. (2003) indicate that the detection probability of H_2 in DLAs increases as soon as log $\kappa > -1.5$. It is clear that all our systems fulfil this condition. Actually Noterdaeme et al. (2018) show that H_2 is present in all systems where the H_2 molecular transitions are covered by our spectra.

Wild & Hewett (2005) indicated that quasars with strong Ca II systems along their line of sight tend to have larger colour excess. In the left panels of Fig. 9 we plot the $W(\text{Ca II}\lambda3934)$ and $W(\text{Na I}\lambda5891)$ as a function of $E(B - V)$. The mean value of Wild & Hewett (2005) is $E(B - V) \sim 0.06$ for $W(\text{Ca II}\lambda3934) \sim 0.55$ Å. It can be seen in the figure that our systems have slightly smaller equivalent widths, albeit errors are large, for the same colour excess.

Correlation between dust reddening and the presence of Ca II and/or Na I absorption lines in our Galaxy has been investigated by Poznanski et al. (2012) and more recently by Murga et al. (2015). The Na I doublet absorption strength in particular is generally expected to correlate with the amount of dust along the line of sight. Richmond et al. (1994) have shown, using 57 high-resolution stellar spectra taken by Sembach et al. (1993), that the equivalent width of individual Na I components correlates with the colour excess measured for these stars, albeit with a noticeable scatter. At lower resolution, the correlation survives although the scatter is even larger due to blending of individual components. Poznanski et al. (2012) combined two samples
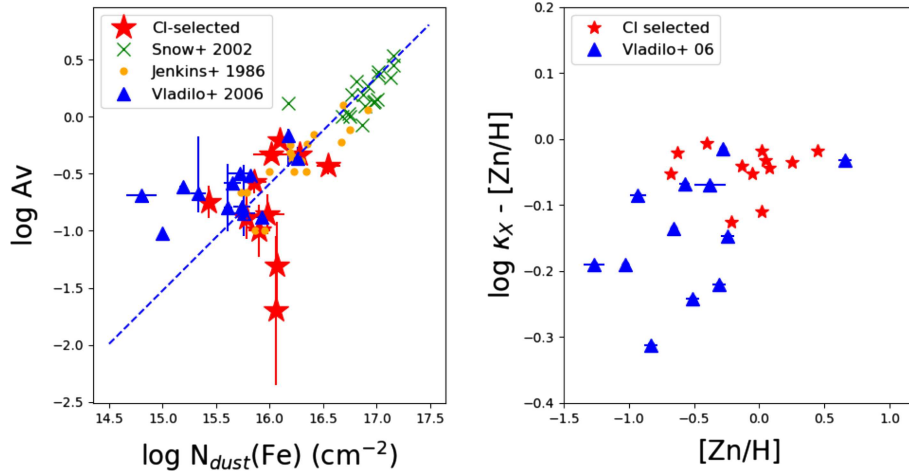
Fig. 8. *Left panel*: attenuation A_V versus the Fe II column density into dust. Red stars are for the C I-selected sample, blue triangles correspond to the data from Vladilo et al. (2006), green crosses and orange points are for samples of local interstellar clouds from Snow et al. (2002) and Jenkins et al. (1986), respectively. The blue dashed line is a linear regression of the Milky Way (MW) data with fixed unit slope (see Vladilo et al. 2006). *Right panel*: the dust-to-gas ratio minus metallicity is plotted against metallicity.
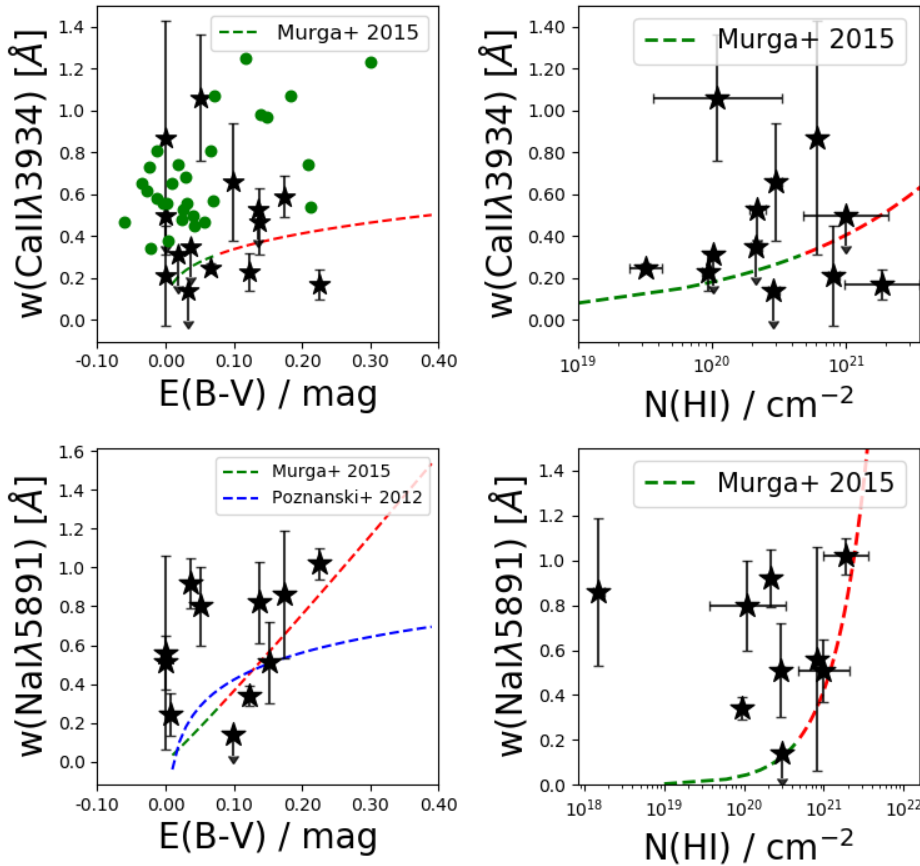
Fig. 9. *Left panels*: $W(Ca\ II\lambda3934)$ in the *upper panel* and $W(Na\ I\lambda5891)$ in the *lower panel* as a function of the colour excess $E(B - V)$. The green dots are the data from Wild & Hewett (2005). In all panels the green dashed lines correspond to the observations of Murga et al. (2015) in the interstellar and circumgalactic media of the Milky Way. The red dashed lines are extrapolations of these relations. The blue line in the $W(Na\ I)$ versus $E(B - V)$ plot is an empirical relation given by Poznanski et al. (2012): $\log(E(B - V)) = 2.16 \times W - 1.91$. *Right panels*: same as left panels with $\log N(H\ I)$ on the x-axis.

of Na I lines observed at high and low resolutions from, respectively, the High Resolution Spectrograph (HIRES) and Echellette Spectrograph and Imager (ESI) spectrographs on the Keck telescope and SDSS and derived an empirical relation between $E(B - V)$ and $W(Na\ I)$. This relation is over-plotted in the left-bottom panel of Fig. 9. It can be seen that our points are not inconsistent with this relation, although $W(Na\ I\lambda5891)$ in C I systems seem to be larger than what is expected.

Murga et al. (2015) used SDSS spectra to obtain mean Na I and Ca II absorptions on the sky and correlate them with $N(H\ I)$ and extinction maps. Both Ca II and Na I absorption strengths

correlate strongly with $N(H\ I)$ and $E(B - V)$, increasing linearly towards higher values until the saturation effect becomes significant at $N(H\ I) \sim 5 \times 10^{20}$ cm^{-2} and $E(B - V) \sim 0.08$ mag. Their relations are over-plotted in Fig. 9.

The dust-to-metal ratio defined as $E(B - V)/N(Zn\ II)$ is plotted versus the Zn II column density in Fig. 10. Values measured in the MW, LMC, and SMC are indicated as horizontal dashed lines. Green points indicate values measured by Wild et al. (2006) in Ca II systems and sub-samples of strong and weak systems. It is noticeable that most of the C I systems have dust-to-metal ratios of the order of what is seen in the MW, LMC, and SMC, with the ex-
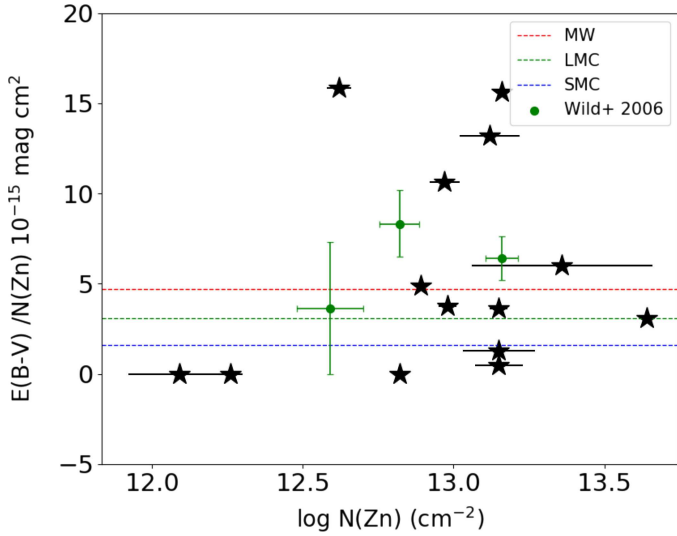
Fig. 10. Dust-to-metal ratio against column density of Zn ɪɪ. Dashed lines indicate values measured in the MW, LMC, and SMC. Green points correspond to values derived in, respectively, all Ca ɪɪ systems and sub-samples of high-*W* value and low-*W* Ca ɪɪ systems by Wild et al. (2006).

ception of four systems, J1133−0057, J2340−0053, J0854+0317, and J1047+2057, which show much larger (by a factor of two to three) values than in the MW. Wild et al. (2006) have already noticed that the values of the dust-to-metal ratios determined for the Ca ɪɪ absorbers were in the range $R_{DM} = (4 − 8) \times 10^{-15}$ mag cm^2, which is often higher than the values derived for the Milky Way. This was particularly true for their strong-system sample including all systems with $W(Ca\,ɪɪ\lambda3934) > 0.7$ Å. Out of the four C ɪ systems with large values, none qualifies for this denomination. The equivalent widths are observed to be in the range 0.17–0.6 Å. We already noticed that the C ɪ system towards J1133−0057 is very peculiar as it is at the redshift of the quasar and arises from a very small cloud (Fathivavsari et al. 2017). Errors are quite large for the system towards J2340−0053 since $E(B − V)$ and $N(Zn\,ɪɪ)$ are small. For the two other systems, there is no apparent explanation. It may be conjectured that dust composition is quite different in these systems and high resolution data may help investigate this issue.

5.2. Nature of the systems

We plot in Fig. 11 the $W(Ca\,ɪɪ\lambda3934)$ (black stars) and $W(Na\,ɪ\lambda5891)$ (red stars) as a function of the $W(C\,ɪ\lambda1560)$. There is a positive correlation for Na ɪ with a linear correlation coefficient of 0.80. This is expected as Na ɪ is seen in cold gas as traced by C ɪ. We note that the correlation can be interpreted as a consequence of an increasing number of components as the equivalent widths increase. If there is a correlation for Ca ɪɪ, it is positive, but there is no strong evidence for it, the linear correlation coefficient being only 0.36. This may indicate that depletion of Ca varies strongly from one system to the other.

The correlation between equivalent widths is seen also between Mg ɪɪ and Mg ɪ (Fig. 12; see also Wild et al. 2006). This is also probably related to the increase of the kinematical extension of the absorptions with increasing rest equivalent width (see Fig. 5).

From the right panels of Fig. 9, we have seen that there is no simple relation between $W(Ca\,ɪɪ\lambda3934)$ and $N(H\,ɪ)$. This has been already emphasized by Nestor et al. (2008) at lower redshift.
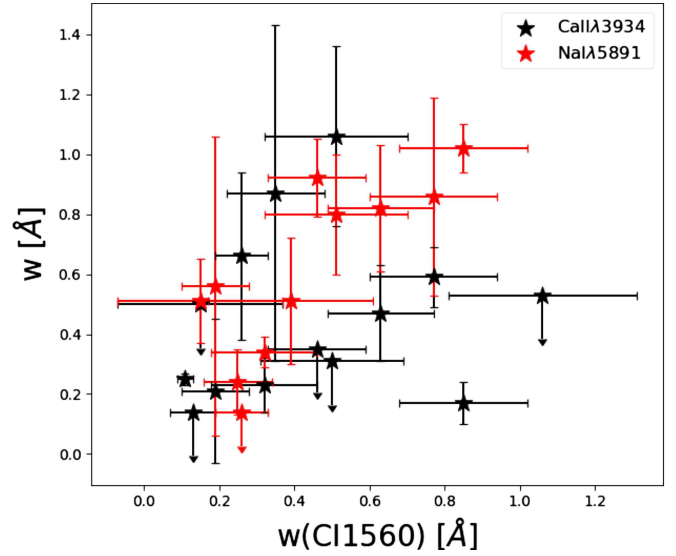
**Fig. 11.** $W(Ca\,ɪɪ\lambda3934)$ (black stars) and $W(Na\,ɪ\lambda5891)$ (red stars) as a function of the $W(C\,ɪ\lambda1560)$.
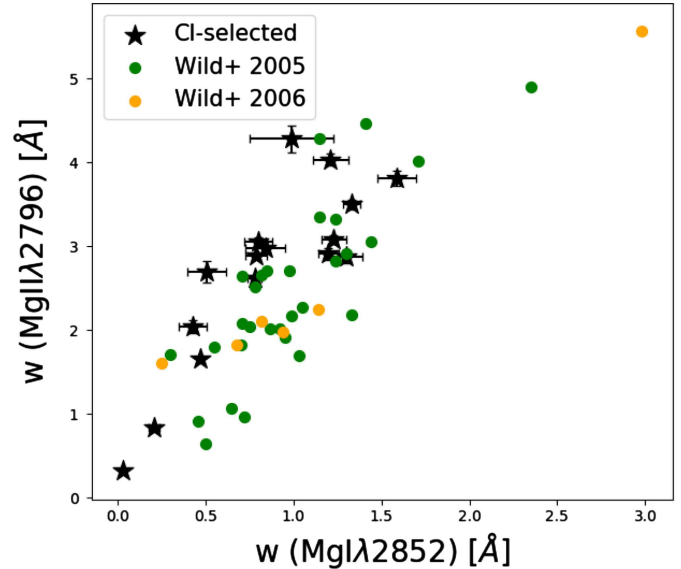
Fig. 12. $W(Mg\,ɪɪ\lambda2796)$ versus $W(Mg\,ɪ\lambda2852)$ equivalent width. The green dots are the data from Wild & Hewett (2005), the orange dots are from Wild et al. (2006).

The latter authors conclude that systems with $W > 0.25$ Å should be DLAs. This conclusion is verified in our sample.

5.2.1. Association with galaxies

Two characteristics of our C ɪ systems are clearly specific, namely that the velocity spread of the Mg ɪɪ absorption is unusually large (nine out of 17 of our systems have $\Delta v > 400\,km\,s^{-1}$; see Fig. 5) and that ten out of 11 of our systems where we could investigate the presence of Na ɪ absorptions have a detection. In Fig. 13 we plot the $W(Mg\,ɪɪ\lambda2796)$ versus the Ca ɪɪ (red stars) and Na ɪ (blue stars) equivalent widths. Data by Wild & Hewett (2005) at lower redshift are over-plotted as green points. It is apparent that the $W(Mg\,ɪɪ\lambda2796)$ measured in our systems are amongst the largest. A trend can be seen in the sense of larger $W(Mg\,ɪɪ\lambda2796)$ for larger $W(Ca\,ɪɪ\lambda3934)$, although the scatter is very large. This may be an indication that
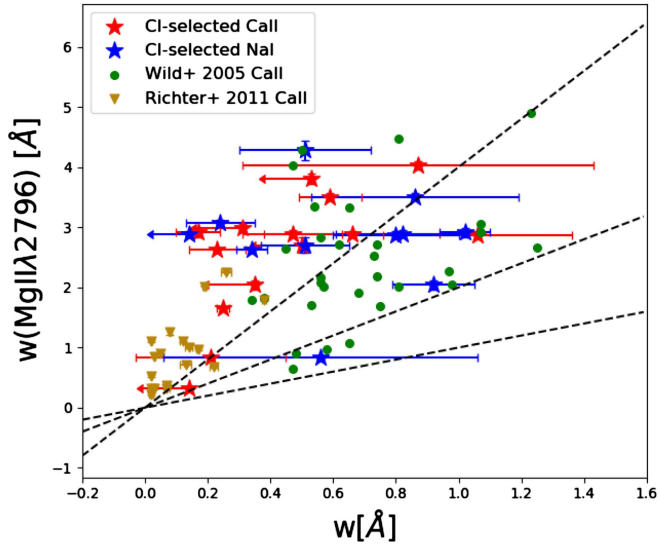
Fig. 13. $W(\text{Mg}\ \textsc{ii}\lambda2796)$ as a function of Ca $\textsc{ii}\lambda3934$ (red stars) and Na $\textsc{i}\lambda5891$ (blue stars) equivalent widths. Green points are from [Wild & Hewett (2005)](#) for systems with $0.6 < z_{\text{abs}} < 1.3$. The orange triangles are the sample from [Richter et al. (2011)](#). The three dashed lines are for $W(\text{MgII})/W(\text{CaII}) = 1$, 2, and 4 respectively.

large $W(\text{Mg}\ \textsc{ii}\lambda2896)$ can be found in a wide variety of situations and in particular at any distance from the associated galaxy. We should note that in the sample of star-forming galaxies in the redshift range 0.4–1.4 observed by [Martin et al. (2012)](#), about 12% have $W(\text{Mg}\ \textsc{ii}\lambda2796) > 2.5\ \text{Å}$ and there is an apparent correlation between the stellar mass and the $W(\text{Mg}\ \textsc{ii}\lambda2796)$.

It is well known that DLAs are not always detected in the disk of galaxies and that the DLA phase is extended towards the halo and even the intergalactic filaments (e.g. [Pontzen et al. 2008](#); [Bouché et al. 2013](#)). This may well be the case as well for the C $\textsc{i}$ systems in our sample.

Several studies have been dedicated to the link between Ca $\textsc{ii}$ systems and associated galaxies at low redshift ([Bowen et al. 1991](#); [Hewett and Wild 2007](#); [Richter et al. 2011](#); [Zych et al. 2007](#)). Galaxies are detected with impact parameters from 5 kpc ([Petitjean et al. 1996](#)) to more than 30 kpc ([Rahmani et al. 2016](#)). In turn, cold gas detected by the presence of molecular hydrogen or very high H $\textsc{i}$ DLA systems seems to be located in the disks of galaxies (see [Noterdaeme et al. 2014](#)). The C $\textsc{i}$ systems studied here are associated with cold gas and Ca $\textsc{ii}$ absorptions but are not always DLAs. It is probable that they arise in different environments. It would therefore be of particular interest to search for the associated galaxies.

5.2.2. C ɪ systems and outflows

We have seen that the C $\textsc{i}$ systems in our sample show very large Mg $\textsc{ii}$ velocity extents. Very large Mg $\textsc{ii}$ absorbers are relatively rare although the large statistics of the SDSS imply that a large number of systems with $W(\text{Mg}\ \textsc{ii}\lambda2796) > 3\ \text{Å}$ is known ([Nestor et al. 2005](#); [Prochter et al. 2006](#); [Quider et al. 2010](#)). By stacking thousands of relatively shallow SDSS images of the fields around strong Mg $\textsc{ii}$ absorption systems, [Zibetti et al. (2007)](#) demonstrated that the strongest systems are associated with bluer galaxies closer to the sightline to the background quasar compared to weaker systems. This suggests a relation between star forming galaxies and strong Mg $\textsc{ii}$ systems, the velocity extent of the latter possibly arising from a

super wind. This is strengthened by the correlation between $W(\text{Mg}\ \textsc{ii})$ and the mean [OII] luminosity in the associated galaxy detected by [Ménard & Chelouche (2009)](#) and [Noterdaeme et al. (2010b)](#). [Joshi et al. (2017)](#) also found that the [OII] luminosity of the galaxy associated with Mg $\textsc{ii}$ systems increases with $W(\text{Mg}\ \textsc{ii})$.

On the other hand, [Nestor et al. (2011)](#) studied two fields of ultra-strong Mg $\textsc{ii}$ systems (J0747+305, $z_{\text{abs}} = 0.7646$, $W(\text{Mg}\ \textsc{ii}\lambda2796) = 3.6\ \text{Å}$ and J1417+011, $z_{\text{abs}} = 0.669$, $W(\text{Mg}\ \textsc{ii}\lambda2796) = 5.6\ \text{Å}$). They detected two galaxies in each field at the same redshift as the absorption at 36 and 61 kpc for J0747+305 and 29 and 58 kpc for J1417+011 from the line of sight to the quasar. This means that either the associated galaxy is at a very small impact parameter and is not seen in the ground-based images or the system can arise at large distances from the host galaxy as suggested in the previous section.

[Bouché et al. (2007)](#) surveyed 21 fields around $z_{\text{abs}} \sim 1$, $W(\text{Mg}\ \textsc{ii}\lambda2796) > 2\ \text{Å}$ systems and detected strong Hα emission in 14 of the fields. The corresponding star-formation rate is in the range 1–20 $M_\odot\ \text{yr}^{-1}$. The impact parameter is <10 kpc for only two of the galaxies and between 11 and 54 kpc for the 12 others.

In our sample, 13 out of 17 systems have $W(\text{Mg}\ \textsc{ii}\lambda2796) > 2\ \text{Å}$ (see Fig. 5). Out of these systems, eight depart from the relation corresponding to a saturated line. This shows that the kinematics is strongly perturbed for most of these systems. It would be surprising if they arose in quiet disks and they must be located close to regions of star-formation activity and/or be part of objects in interaction. However, [Bouché et al. (2012)](#) searched the fields of 20 strong ($W(\text{Mg}\ \textsc{ii}\lambda2796) > 2\ \text{Å}$) $z \sim 2$ Mg $\textsc{ii}$ systems for star-formation activity and detected only four of them. This may indicate that not all strong Mg $\textsc{ii}$ systems are related to strong star-formation activity. Since our systems contain cold gas, it would be most interesting to search for the counterparts of star-formation activity around the systems in our sample. As noticed before, we found three systems in the spectra of J1047+2057, J1133−0057, and J2350−0052 where the Mg $\textsc{ii}$ absorptions show two distinct saturated sub-systems separated by more than 200 km s^{-1} in the C $\textsc{i}$ and Mg $\textsc{ii}$ absorption profiles. In J1133−0057, we detected also two distinct Na $\textsc{i}$ components. This is a small but significant fraction of the sample where it is reasonable to believe that the systems arise in interacting objects. We should note that in the case of J2350−0052, [Krogager et al. (2017)](#) detect Ly-α emission at an impact parameter of ~ 6 kpc. In any case, all this suggests that a large fraction of the cold gas at high redshift arises in disturbed environments probably in places with strong star-formation activity.

6. Conclusion

In this paper we have studied a sample of 17, $z_{\text{abs}} > 1.5$, absorption systems selected only on the basis of the presence of C $\textsc{i}$ absorption in the SDSS spectrum of background quasars ([Ledoux et al. 2015](#)) and observed with the ESO spectrograph X-shooter. The $W(\text{C}\ \textsc{i}\lambda1656)$ are in the range 0.17 to 1.42 Å. Thanks to the large wavelength coverage of the X-shooter instrument, we can study, for the first time at these high redshifts, the Ca $\textsc{ii}\lambda\lambda3934,3969$ and Na $\textsc{i}\lambda\lambda5891,5897$ absorption together with Mg $\textsc{ii}$ and Mg $\textsc{i}$ absorptions.

We show that most of these systems have high metallicities and dust content compared to standard DLAs at these redshifts. We detect nine Ca $\textsc{ii}$ absorptions with $W(\text{Ca}\ \textsc{ii}\lambda3934) > 0.23\ \text{Å}$ out of 13 systems where we could have

observed the line. The observed equivalent widths are similar to what is observed in other lower redshift surveys. We detect ten Na ɪ absorptions out of 11 systems where we could observe this species. No trend is seen between either W(Ca ɪɪ) or W(Na ɪ) and metallicity. While most of the systems have dust-to-metal ratios of the order of what is seen in the Milky Way, Large, and Small Magellanic Clouds, four of the systems have values two or three times larger than what is observed in the Milky Way. Although the errors affecting our estimates are still large, this may be an indication that these C ɪ systems are at an advanced stage of chemical evolution. There is, however, no indication that the systems with large dust-to-metal ratios are a peculiar subset of the overall sample.

The systematic presence of Na ɪ in these C ɪ systems indicates that they probably probe the cold gas in the ISM of high-redshift galaxies. The characteristics of the systems are such that most of the systems should show molecular hydrogen. This will be confirmed in an associated paper (Noterdaeme et al. 2018).

Most of the systems (12 out of 17) have W(Mg ɪɪ$\lambda2796$) > 2.5 Å. The Mg ɪɪ absorptions are spread over more than ~400 km s^{-1} for half of the systems; three absorbers have an extension larger than 500 km s^{-1}. This is reminiscent of the detection of molecular hydrogen (log N(H$_2$) = 17.4 and 16.5) in Q0551−366 and Q0013−004, where the Mg ɪɪ absorptions are spread over $\Delta v \sim 700$ and 1000 km s^{-1}, respectively, for a metallicity relative to solar [Zn/H] = −0.13 and −0.02 and W(C ɪ) ~ 0.25 and 0.33 Å (Ledoux et al. 2002; Petitjean et al. 2002). These large velocities can be the consequence of either interaction or star-formation activity in the associated galaxy or cold flow disks (Stewart et al. 2013). Ledoux et al. (2006) have interpreted the observed correlation between Δv and metallicity in DLAs as a tracer of an underlying mass-metallicity relation. This is based on the assumption that Δv is a tracer of the virial velocity and thus the halo mass. Others have interpreted large velocities as the consequences of strong winds powered by star formation (e.g. Bouché et al. 2016). We note that both interpretations would imply that if the kinematics is strongly perturbed for most of these systems, the winds probably do not arise in quiet disks and are located close to regions of intense star-formation activity and/or are part of objects in interaction. However, Bouché et al. (2012) searched the fields of 20 strong (W(Mg ɪɪ$\lambda2796$) > 2 Å) $z \sim 2$ Mg ɪɪ systems for star-formation activity and detected only four of them. This may indicate that not all strong Mg ɪɪ systems are related to strong star-formation activity. Since our systems contain cold gas, it would be most interesting to search for their optical counterparts and associated star-formation activity in emission.

References

Abazajian, K. N., Adelman-McCarthy, J. K., Agüeros, M. A., et al. 2009, ApJS, 182, 543

Balashev, S. A., Petitjean, P., Ivanchik, A. V., et al. 2011, MNRAS, 418, 357

Balashev, S. A., Noterdaeme, P., Klimenko, V. V., et al. 2015, A&A, 575, L8

Balashev, S. A., Noterdaeme, P., Rahmani, H., et al. 2017, MNRAS, 470, 2890

Bekhti, N. B., Murphy, M., Richter, P., et al. 2008, Astrophys. Space Sci. Proc., 5, 273

Ben Bekhti, N., Winkel, B., Richter, P., et al. 2012, A&A, 542, A110

Berg, T. A. M., Ellison, S. L., Prochaska, J. X., Venn, K. A., & Dessauges-Zavadsky, M. 2015, MNRAS, 452, 4326

Berg, T. A. M., Ellison, S. L., Sánchez-Ramírez, R., et al. 2016, MNRAS, 463, 3021

Blades, J. C., Turnshek, D. A., & Norman, C. A. 1988, Proc. of the QSO Absorption Line Meeting (Cambridge University Press)

Boissé, P. 1995, in QSO Absorption Lines, ed. G. Meylan, 35

Boissé, P., Bergeron, J., Prochaska, J. X., Péroux, C., & York, D. G. 2015, A&A, 581, A109

Bouché, N., Murphy, M. T., Péroux, C., et al. 2007, ApJ, 669, L5

Bouché, N., Murphy, M. T., Péroux, C., et al. 2012, MNRAS, 419, 2

Bouché, N., Murphy, M. T., Kacprzak, G. G., et al. 2013, Science, 341, 50

Bouché, N., Finley, H., Schroetter, I., et al. 2016, ApJ, 820, 121

Bowen, D. V., Pettini, M., Penston, M. V., & Blades, C. 1991, MNRAS, 249, 145

Carswell, R. F., & Webb, J. K. 2014, Astrophysics Source Code Library [record ascl:1408.015]

Cherinka, B., & Schulte-Ladbeck, R. E. 2011, AJ, 142, 122

Cox, N. L. J., Cordiner, M. A., Ehrenfreund, P., et al. 2007, A&A, 470, 941

Cui, J., Bechtold, J., Ge, J., & Meyer, D. M. 2005, ApJ, 633, 649

Daprà, M., Niu, M. L., Salumbides, E. J., Murphy, M. T., & Ubachs, W. 2016, ApJ, 826, 192

Ellison, S. L. 2006, MNRAS, 368, 335

Fathivavsari, H., Petitjean, P., Zou, S., et al. 2017, MNRAS, 466, L58

Ferlet, R., Vidal-Madjar, A., & Gry, C. 1985, ApJ, 298, 838

Fynbo, J. P. U., Ledoux, C., Noterdaeme, P., et al. 2011, MNRAS, 413, 2481

Ge, J., & Bechtold, J. 1997, ApJ, 477, L73

Ge, J., & Bechtold, J. 1999, ASP Conf. Ser., 156, 121

Gordon, K. D., Clayton, G. C., Misselt, K. A., Landolt, A. U., & Wolff, M. J. 2003, ApJ, 594, 279

Guber, C. R., & Richter, P. 2016, A&A, 591, A137

Hall, P. B., Anderson, S. F., Strauss, M. A., et al. 2002, ApJS, 141, 267

Hewett, P. C., & Wild, V. 2007, MNRAS, 379, 738

Hobbs, L. M. 1974, ApJ, 191, 381

Hobbs, L. M. 1975, ApJ, 202, 628

Jenkins, E. B., Savage, B. D., & Spitzer, Jr., L. 1986, ApJ, 301, 355

Jorgenson, R. A., Murphy, M. T., Thompson, R., & Carswell, R. F. 2014, MNRAS, 443, 2783

Joshi, R., Srianand, R., Noterdaeme, P., & Petitjean, P. 2017, MNRAS, 465, 701

Keenan, F. P., Dufton, P. L., McKeith, C. D., & Blades, J. C. 1983, MNRAS, 203, 963

Krogager, J.-K., Geier, S., Fynbo, J. P. U., et al. 2015, ApJS, 217, 5

Krogager, J.-K., Møller, P., Fynbo, J. P. U., & Noterdaeme, P. 2017, MNRAS, 469, 2959

Kunth, D., & Bergeron, J. 1984, MNRAS, 210, 873

Ledoux, C., Srianand, R., & Petitjean, P. 2002, A&A, 392, 781

Ledoux, C., Petitjean, P., & Srianand, R. 2003, MNRAS, 346, 209

Ledoux, C., Petitjean, P., Fynbo, J. P. U., Møller, P., & Srianand, R. 2006, A&A, 457, 71

Ledoux, C., Noterdaeme, P., Petitjean, P., & Srianand, R. 2015, A&A, 580, A8

López, S., D'Odorico, V., Ellison, S. L., et al. 2016, A&A, 594, A91

Ma, J., Caucal, P., Noterdaeme, P., et al. 2015, MNRAS, 454, 1751

Martin, C. L., Shapley, A. E., Coil, A. L., et al. 2012, ApJ, 760, 127

Ménard, B., & Chelouche, D. 2009, MNRAS, 393, 808

Modigliani, A., Goldoni, P., Royer, F., et al. 2010, in Observatory Operations: Strategies, Processes, and Systems III, Proc. SPIE, 7737, 773728

Murga, M., Zhu, G., Ménard, B., & Lan, T.-W. 2015, MNRAS, 452, 511

Nestor, D. B., Turnshek, D. A., & Rao, S. M. 2005, ApJ, 628, 637

Nestor, D. B., Pettini, M., Hewett, P. C., Rao, S., & Wild, V. 2008, MNRAS, 390, 1670

Nestor, D. B., Johnson, B. D., Wild, V., et al. 2011, MNRAS, 412, 1559

Noterdaeme, P., Ledoux, C., Petitjean, P., & Srianand, R. 2008, A&A, 481, 327

Noterdaeme, P., Petitjean, P., Ledoux, C., et al. 2010a, A&A, 523, A80

Noterdaeme, P., Srianand, R., & Mohan, V. 2010b, MNRAS, 403, 906

Noterdaeme, P., Petitjean, P., Srianand, R., Ledoux, C., & López, S. 2011, A&A, 526, L7

Noterdaeme, P., Laursen, P., Petitjean, P., et al. 2012a, A&A, 540, A63

Noterdaeme, P., Petitjean, P., Carithers, W. C., et al. 2012b, A&A, 547, L1

Noterdaeme, P., Petitjean, P., Pâris, I., et al. 2014, A&A, 566, A24

Noterdaeme, P., Petitjean, P., & Srianand, R. 2015, A&A, 578, L5

Noterdaeme, P., Ledoux, C., Zou, S., et al. 2018, A&A, 612, A58

Petitjean, P., Theodore, B., Smette, A., & Lespine, Y. 1996, A&A, 313, L25

Petitjean, P., Aracil, B., Srianand, R., & Ibata, R. 2000a, A&A, 359, 457

Petitjean, P., Srianand, R., & Ledoux, C. 2000b, A&A, 364, L26

Petitjean, P., Srianand, R., & Ledoux, C. 2002, MNRAS, 332, 383

Pontzen, A., Governato, F., Pettini, M., et al. 2008, MNRAS, 390, 1349

Poznanski, D., Prochaska, J. X., & Bloom, J. S. 2012, MNRAS, 426, 1465

Prochter, G. E., Prochaska, J. X., & Burles, S. M. 2006, ApJ, 639, 766

Quider, A. M., Shapley, A. E., Pettini, M., Steidel, C. C., & Stark, D. P. 2010, MNRAS, 402, 1467

Rafelski, M., Neeleman, M., Fumagalli, M., Wolfe, A. M., & Prochaska, J. X. 2014, ApJ, 782, L29

Rahmani, H., Péroux, C., Turnshek, D. A., et al. 2016, MNRAS, 463, 980

Rao, S. M., Prochaska, J. X., Howk, J. C., & Wolfe, A. M. 2005, AJ, 129, 9

Richmond, M. W., Treffers, R. R., Filippenko, A. V., et al. 1994, AJ, 107, 1022

Richter, P., Krause, F., Fechner, C., Charlton, J. C., & Murphy, M. T. 2011, A&A, 528, A12

Routly, P. M., & Spitzer, Jr., L. 1952, ApJ, 115, 227

Sardane, G. M., Turnshek, D. A., & Rao, S. M. 2014, MNRAS, 444, 1747

Sardane, G. M., Turnshek, D. A., & Rao, S. M. 2015, MNRAS, 452, 3192

Schneider, D. P., Richards, G. T., Hall, P. B., et al. 2010, AJ, 139, 2360

Selsing, J., Fynbo, J. P. U., Christensen, L., & Krogager, J.-K. 2016, A&A, 585, A87

Sembach, K. R., Danks, A. C., & Savage, B. D. 1993, A&AS, 100, 107

Snow, T. P. & McCall, B. J. 2006, ARA&A, 44, 367

Snow, T. P., Rachford, B. L., & Figoski, L. 2002, ApJ, 573, 662

Srianand, R., Petitjean, P., Ledoux, C., Ferland, G., & Shaw, G. 2005, MNRAS, 362, 549

Srianand, R., Gupta, N., Petitjean, P., et al. 2012, MNRAS, 421, 651

Stewart, K. R., Brooks, A. M., Bullock, J. S., et al. 2013, ApJ, 769, 74

Vernet, J., Dekker, H., D'Odorico, S., et al. 2011, A&A, 536, A105

Vestergaard, M., & Wilkes, B. J. 2001, ApJS, 134, 1

Vladilo, G., Molaro, P., Monai, S., et al. 1993, A&A, 274, 37

Vladilo, G., Centurión, M., Levshakov, S. A., et al. 2006, A&A, 454, 151

Vollmann, K., & Eversberg, T. 2006, Astron. Nachr., 327, 862

Wakker, B. P., & Mathis, J. S. 2000, ApJ, 544, L107

Wang, T. G., Dong, X. B., Zhou, H. Y., & Wang, J. X. 2005, ApJ, 622, L101

Welty, D. E., & Hobbs, L. M. 2001, ApJS, 133, 345

Welty, D. E., Hobbs, L. M., & Kulkarni, V. P. 1994, ApJ, 436, 152

Welty, D. E., Morton, D. C., & Hobbs, L. M. 1996, ApJS, 106, 533

Wild, V., & Hewett, P. C. 2005, MNRAS, 361, L30

Wild, V., Hewett, P. C., & Pettini, M. 2006, MNRAS, 367, 211

Wiseman, P., Schady, P., Bolmer, J., et al. 2017, A&A, 599, A24

Wolfe, A. M., & Prochaska, J. X. 2000, ApJ, 545, 591

Womble, D. S., Junkkarinen, V. T., Cohen, R. D., & Burbidge, E. M. 1990, AJ, 100, 1785

Zibetti, S., Ménard, B., Nestor, D. B., et al. 2007, ApJ, 658, 161

Zych, B. J., Murphy, M. T., Pettini, M., et al. 2007, MNRAS, 379, 1409

Zych, B. J., Murphy, M. T., Hewett, P. C., & Prochaska, J. X. 2009, MNRAS, 392, 1429

## Appendix A: Comments on individual systems

We use here the notations Ca ɪɪ K and H for Ca ɪɪλ3934Å and Ca ɪɪλ3969Å, respectively, Na ɪ D for the Na ɪ$\lambda\lambda$5891,5897 doublet, and W for the rest equivalent width. The neutral carbon ground base fine structure levels are denoted as C ɪ, C ɪ*, and C ɪ** for the $2s^2 2p^{2\,3}P_J^e$ levels where $J = 0,1,2$.

(a)

(b)
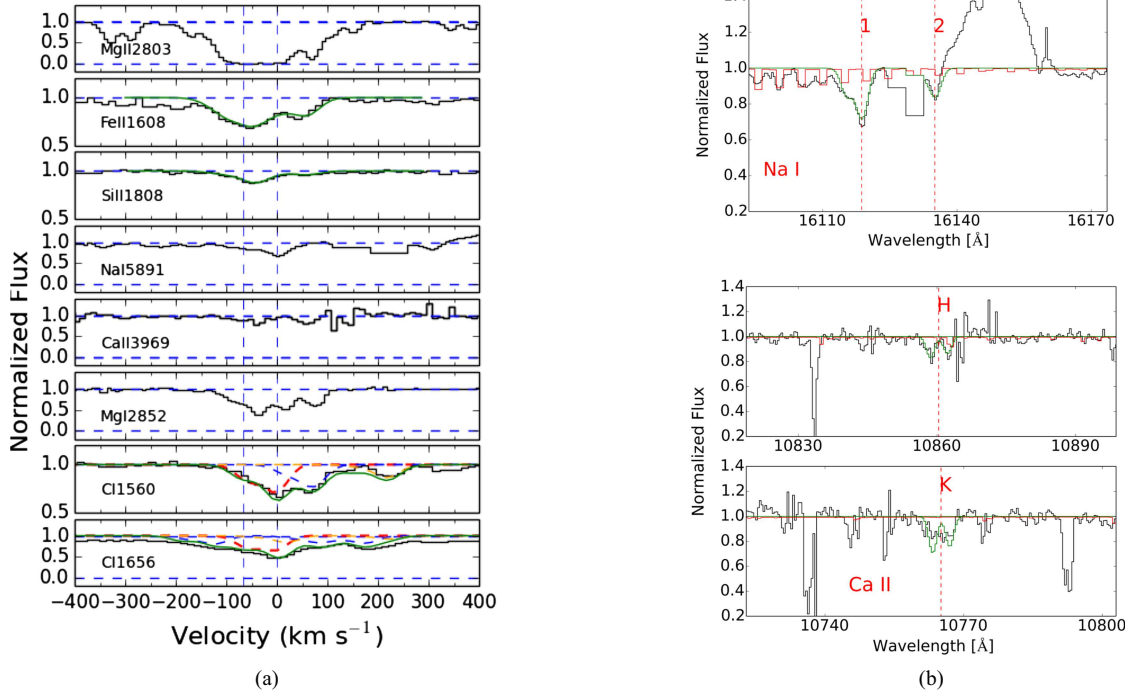
Fig. A.1. J0216−0021 : *left panels (a)*: velocity plot of a sub-set of the absorbing species. The vertical dashed lines indicate the positions of the C ɪ components. Fits to the absorption profiles are over-plotted with the data. For C ɪ transitions, the red dashed line corresponds to the true ground state, the blue dashed line is for the C ɪ* absorption, and the orange dashed line is for the C ɪ** absorption. The redshift is taken in Table 1 to give the zero velocity. *Right panels (b)*: upper panel is the spectrum at the expected position of Na ɪ$\lambda\lambda$5891,5897, the 1 and 2 indicate the Na ɪλ5891 and Na ɪλ5897 lines respectively; lower panel is the spectrum at the expected positions of the Ca ɪɪ$\lambda\lambda$3934,3969 lines, the H and K notations indicate the Ca ɪɪλ3969 and Ca ɪɪλ3934 lines respectively. The red curve is the telluric spectrum template of X-shooter: In this system the Ca ɪɪ K line is clearly detected but we indicate an upper limit for the H line since the data around the H line is noisy (see Fig. A.1b lower panel). The Na ɪ D is detected clearly even though there are strong spikes close to the two absorption lines (see Fig. A.1b upper panel). We subtracted the equivalent width of the weak telluric contamination. The C ɪλ1560 line is not used in the fit of the C ɪ absorption as it is strongly blended. There are two components at $z = 1.735283$ and 1.735888, while the strongest component of Fe ɪɪ, Si ɪɪ, and Mg ɪ is seen in-between these two components (see also J1248+2848). This could be an artefact due to the spectral resolution. To discuss the details of the structure of the absorbing cloud, higher resolution data are needed.

(a)

(b)
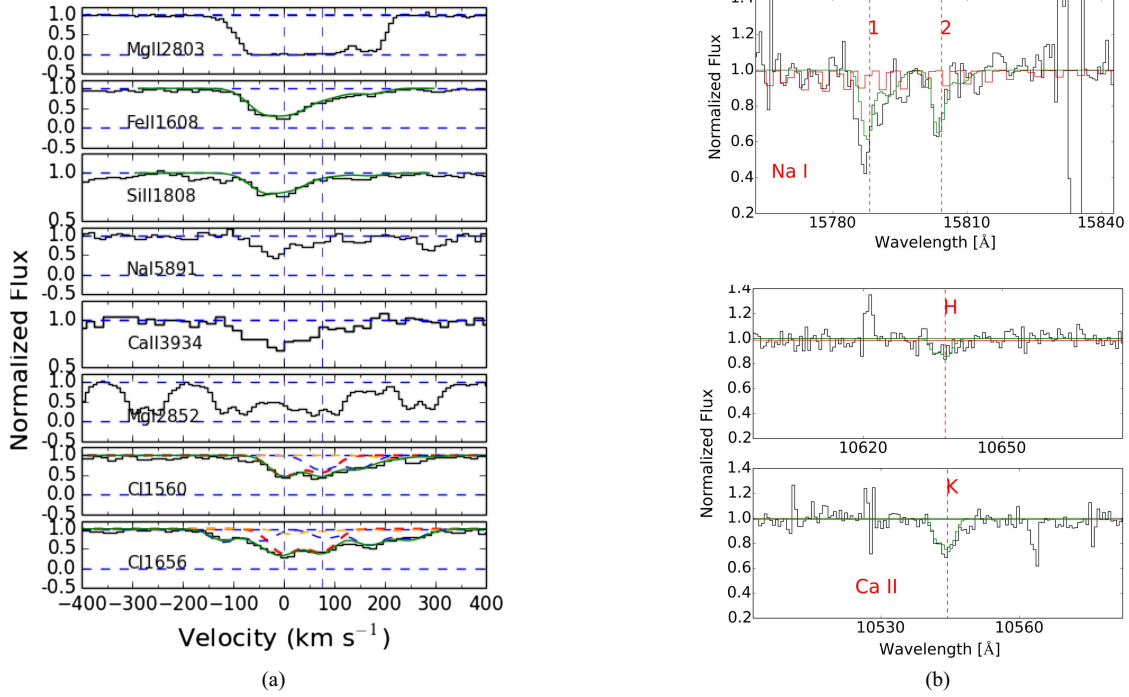
Fig. A.2. J0815+2640: The Ca II H and Na I D lines are clearly detected. We conservatively give an upper limit for the Ca II H line in Table 2. The Na I D line is somehow blended with telluric absorptions. We therefore have subtracted the sky contamination from the EW. The Mg Iλ2852 feature is strongly blended with absorption from the sky. Weak lines from the Ni II triplet are detected.

(a)

(b)
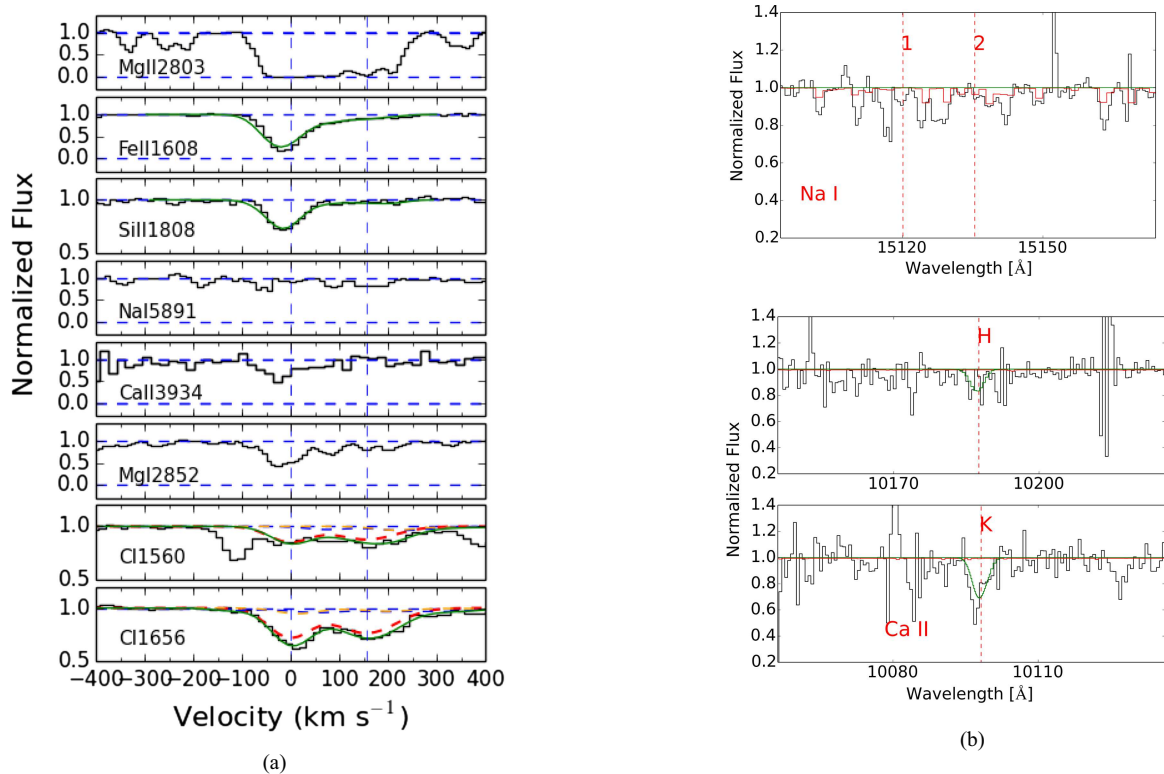
Fig. A.3. J0854+0317: The Ca II K line is detected in this system, when the Ca II H line is lost in the noise. The spectrum around the expected position of Na I D is relatively good but no absorption is seen down to 0.23 Å. There is a slight shift of ∼−25 km s^{-1} between the strongest component of Fe II and Si II and the strongest C Iλ1656 component. The C Iλ1560 line is blended with other lines at ∼−125 km s^{-1} and 400 km s^{-1}. Weak lines of Zn II and Mn II are detected.

(a)   (b)
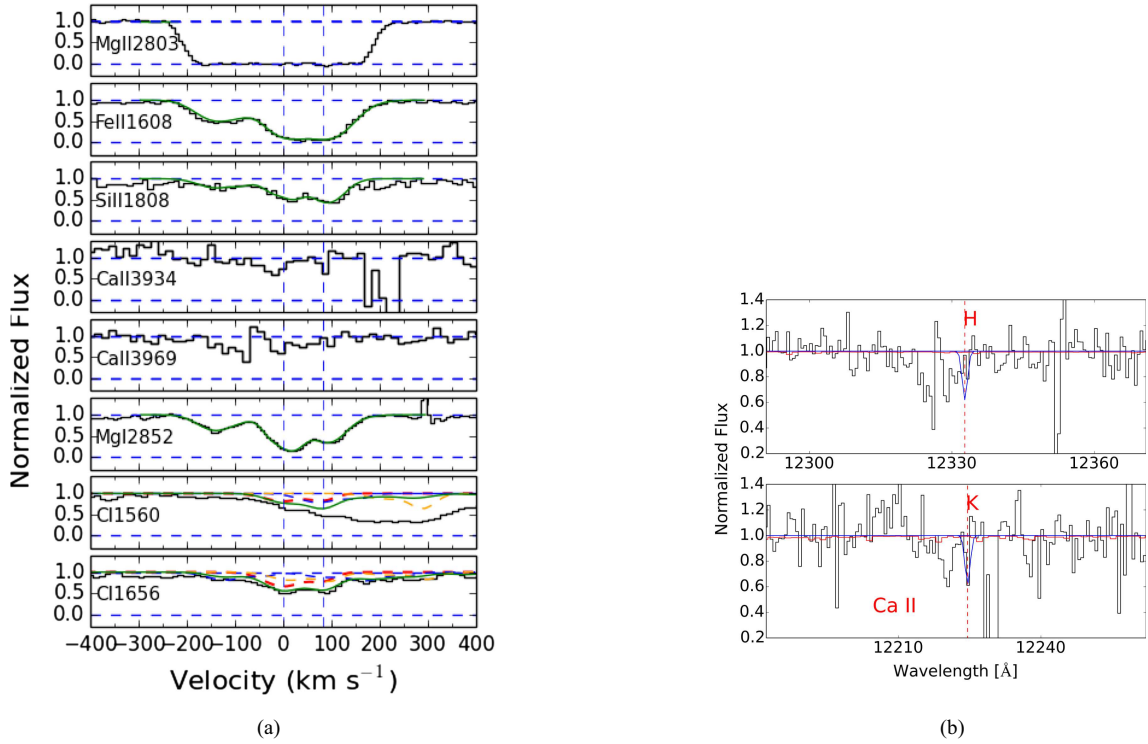
Fig. A.4. J0917+0154: Data are noisy at the expected positions of Ca II H&K. The Na I D is redshifted in the gap between the H and K bands. The Ni II and Zn II lines are also detected. There is no obvious CO line detection in the X-shooter spectrum. The C I λ1560 line is strongly blended, therefore we did not include it in our fit.

(a)   (b)
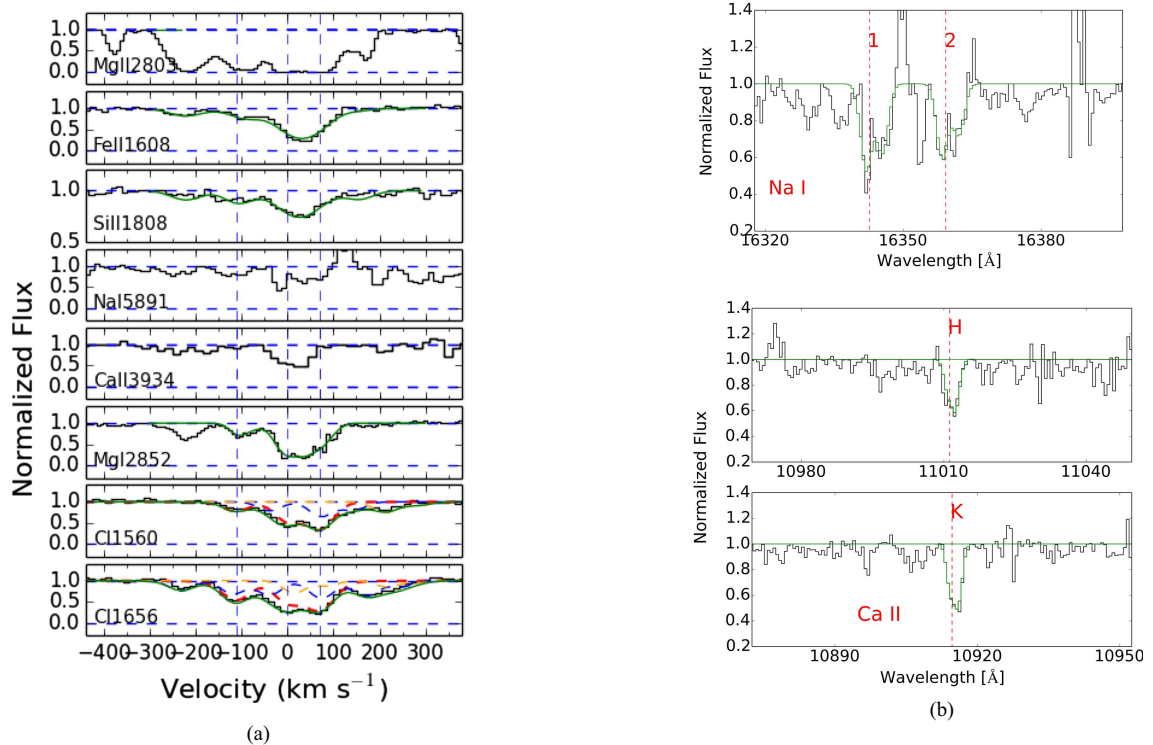
Fig. A.5. J1047+2057: Both Ca II H&K and Na I D are detected and strong. The spectrum around Na I D is noisy however, thus the error on EW is relatively large. The redshift defined by the strongest C I component does not correspond to the exact centre of the Na I D lines. The strongest component of Na I D is shifted by around 25 km s^{-1} compared to C I. This may be an artefact of the intermediate resolution of X-shooter as the C I fit is complex and needs at least three components. Higher resolution data are needed to study in more detail the structure of the absorbing cloud. The elements H$_2$ and CO are detected. Mg II for this system is uncommonly strong and spans around 800 km s^{-1} including components at -350 km s^{-1} and $+400$ km s^{-1}. Noterdaeme et al. (2010a) first detected CO in this system and used it to measure the cosmic microwave background (CMB) temperature at the corresponding redshift. They obtain a column density of log N(CO) = 14.74 ± 0.07. From the X-shooter data we derive log N(CO) = 14.56 ± 0.92, which is in agreement with the result by Noterdaeme et al. (2011). Daprà et al. (2016) used the CO absorption from this system to constrain the cosmological variation of the proto-to-electron mass ratio. NiII and ZnII are detected.

(a)

(b)
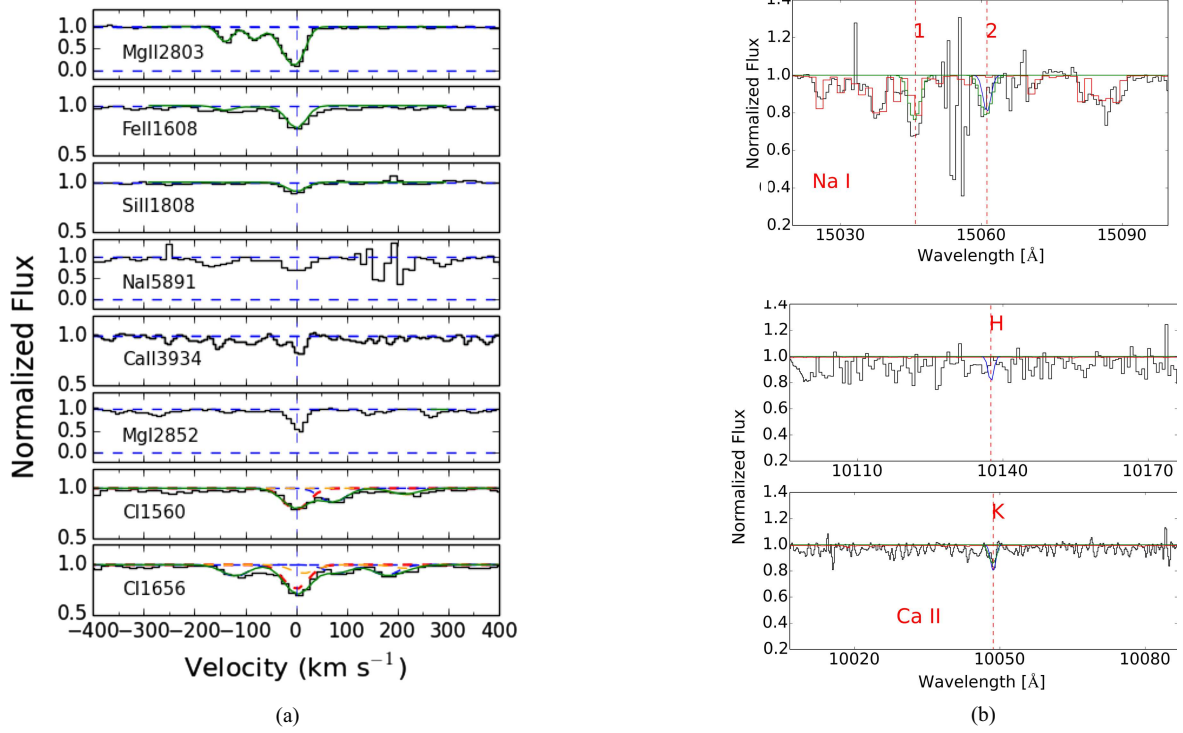
Fig. A.6. J1122+1437: In this spectrum Ca II and Na I are both detected. The Ca II K line is clearly detected but not Ca II H (see Table 2). For the Na I D doublet, both lines are detected. However, Na I λ5891 is strongly blended with a telluric feature but there is an apparent excess that can be estimated and subtracted (Fig. A.6b upper panel). Metal lines and C I absorptions are detected in one strong component plus several weaker components blueshifted by -170, -100, and $-20\,\mathrm{km\,s^{-1}}$ relative to the main component.

(a)

(b)
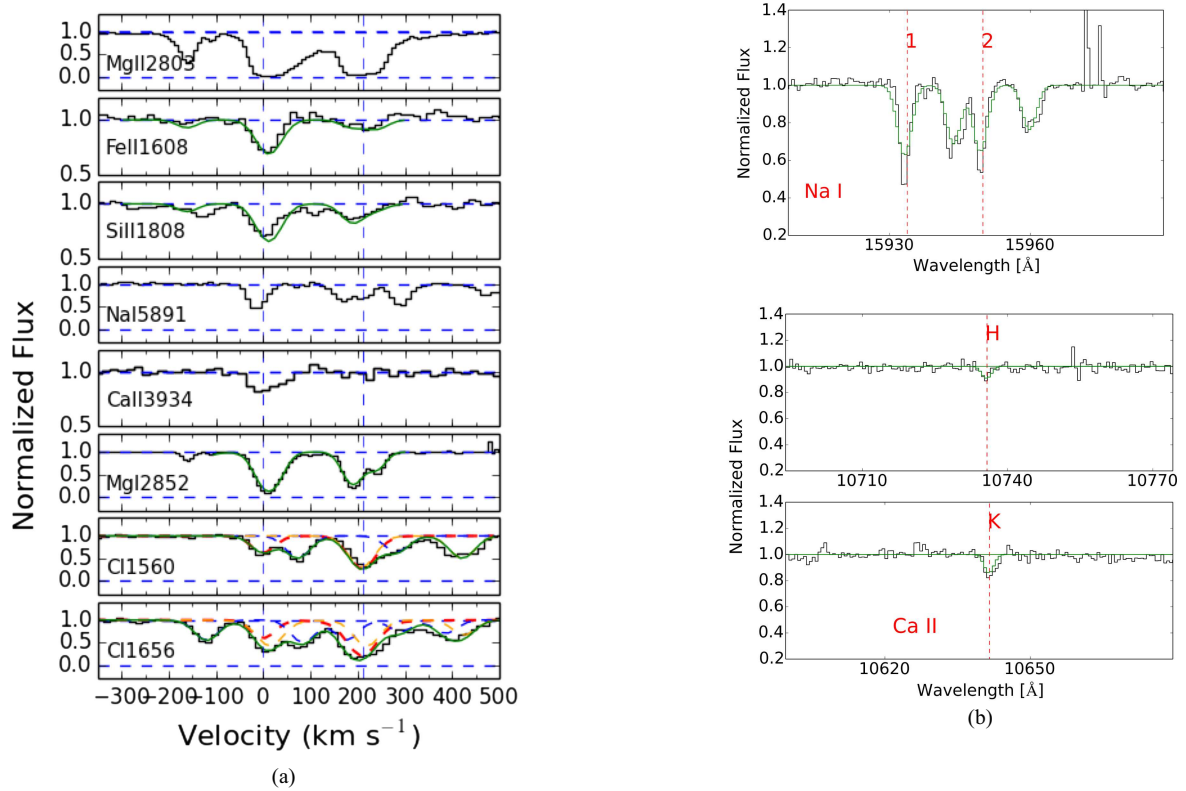
Fig. A.7. J1133−0057: Both Ca II H&K and Na I D are clearly detected in this good spectrum. This system is a peculiar but interesting case for which the absorbing cloud is small and located at a short distance to the quasar. Indeed, the broad line region (BLR) is only partially covered by the cloud. This system has been analysed by Fathivavsari et al. (2017) who derived an H I column density of 21.00 ± 0.30. There are two main components separated by $\sim$200 km s^{-1}. Although Ca II is detected only in the strongest system, Na I is detected in both. Ca must be highly depleted into dust, which is consistent with the corresponding large attenuation of the quasar (see Table 3).

(a)

(b)
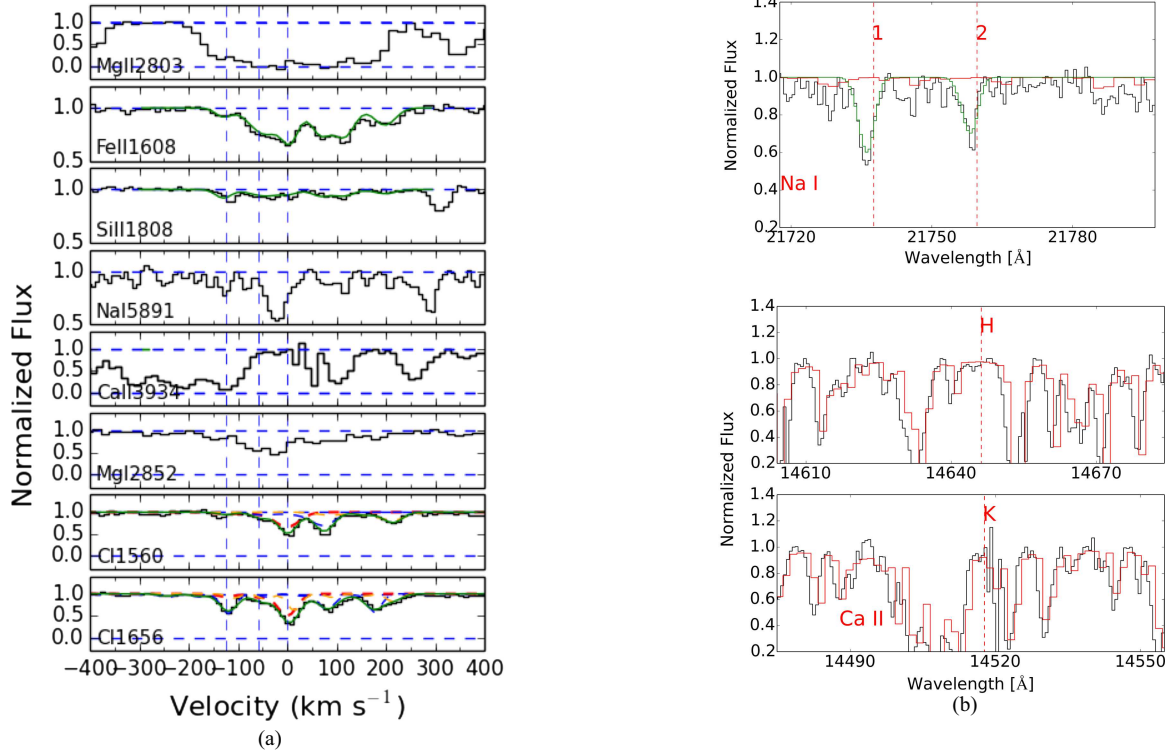
Fig. A.8. J1237+0647: In this spectrum Na ɪ D is clearly detected while Ca ɪɪ H& K are strongly blended with telluric absorptions, so there is no EW upper limit for Ca ɪɪ D. Detection of H_2 and CO in this system has been published by Noterdaeme et al. (2010a). The excitation of the CO rotational levels is used to measure T_{CMB}. The spectrum used by Noterdaeme et al. (2010a) was obtained with UVES and the authors derive log N(HI) = 20.0 ± 0.15, to be compared with our measurement 19.89 ± 0.47. The system is also analysed by Daprà et al. (2016). Three components are used to fit the absorptions from C ɪ and its fine structure lines. The components of Fe ɪɪ and C ɪ are in exactly the same place.

(a)

(b)
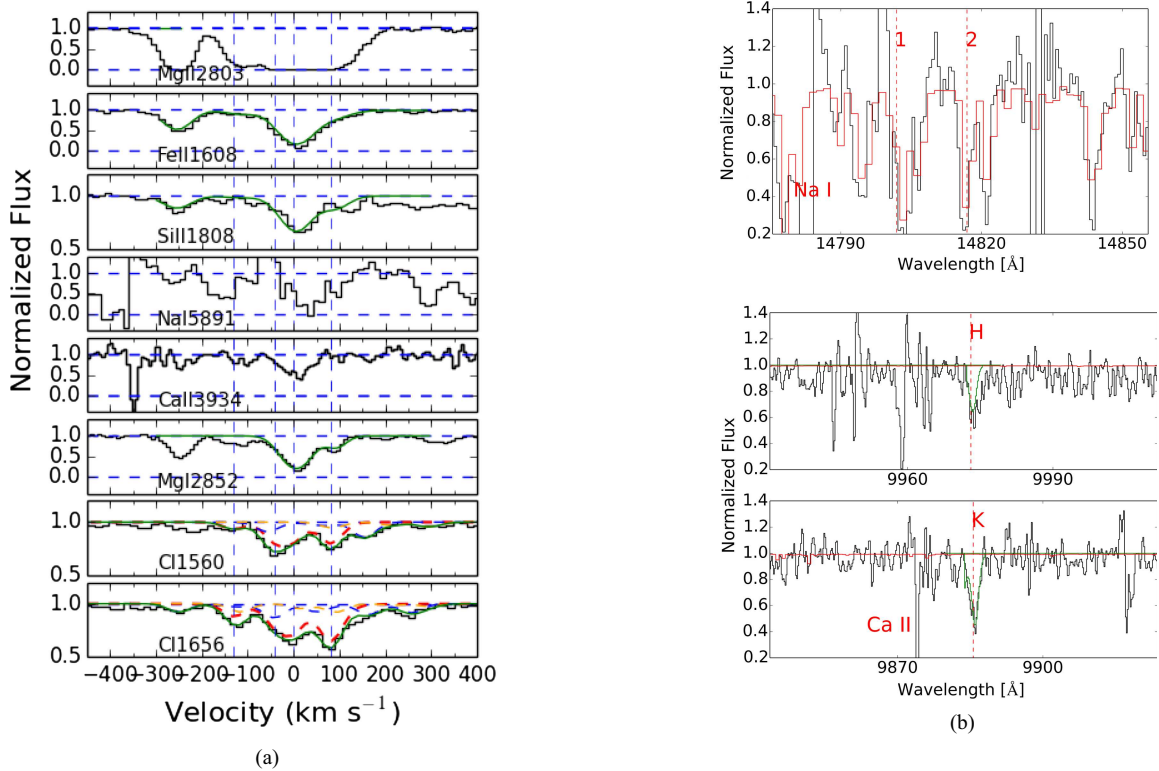
Fig. A.9. J1248+2848: Both Ca ɪɪ K & H lines are detected for this system. The Ca ɪɪ H line is, however, blended with a sky feature, thus the value given in Table 2 for the *EW* Ca ɪɪ H line is somewhat tentative. As in the case of J1346+0644, Na ɪ D lines are badly blended with strong telluric absorptions. This is why we do not give an *EW* upper limit for Na ɪ D. The component at $v \sim -250$ km s^{-1} is included into the fit and the measurement of W(Mg ɪλ2852). The width of the metal line absorption profile is around 575 km s^{-1}.

(a)

(b)
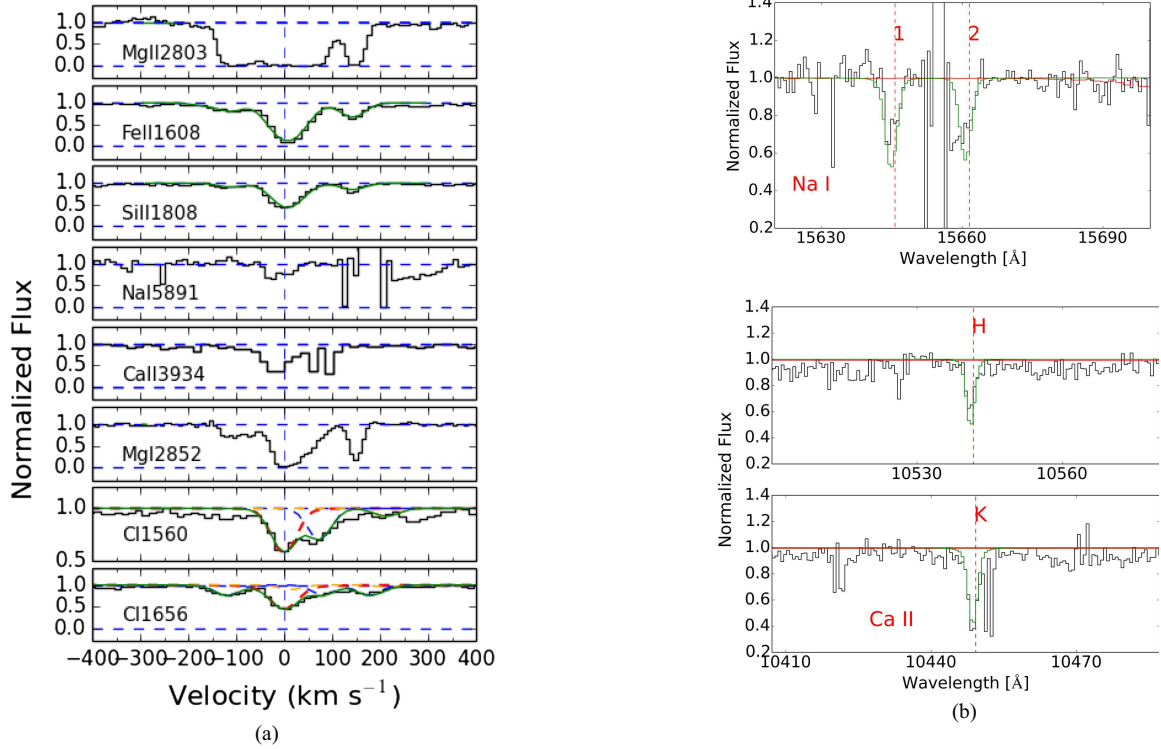
Fig. A.10. J1302+2111: Both Na ɪ and Ca ɪɪ are detected for this system. The Na ɪλ5891 line is clean, However, there is a spike close to Na ɪλ5897 that prevents a direct measurement of the *EW*. We thus fit the doublet using VPFIT to derive the *EW* for Na ɪλ5897. The Fe ɪɪλ2586 and Fe ɪɪλ2600 lines are strongly blended with sky absorptions, so we did not use them to fit the Fe ɪɪ lines. C ɪ is well fitted with one component.


(a)

(b)
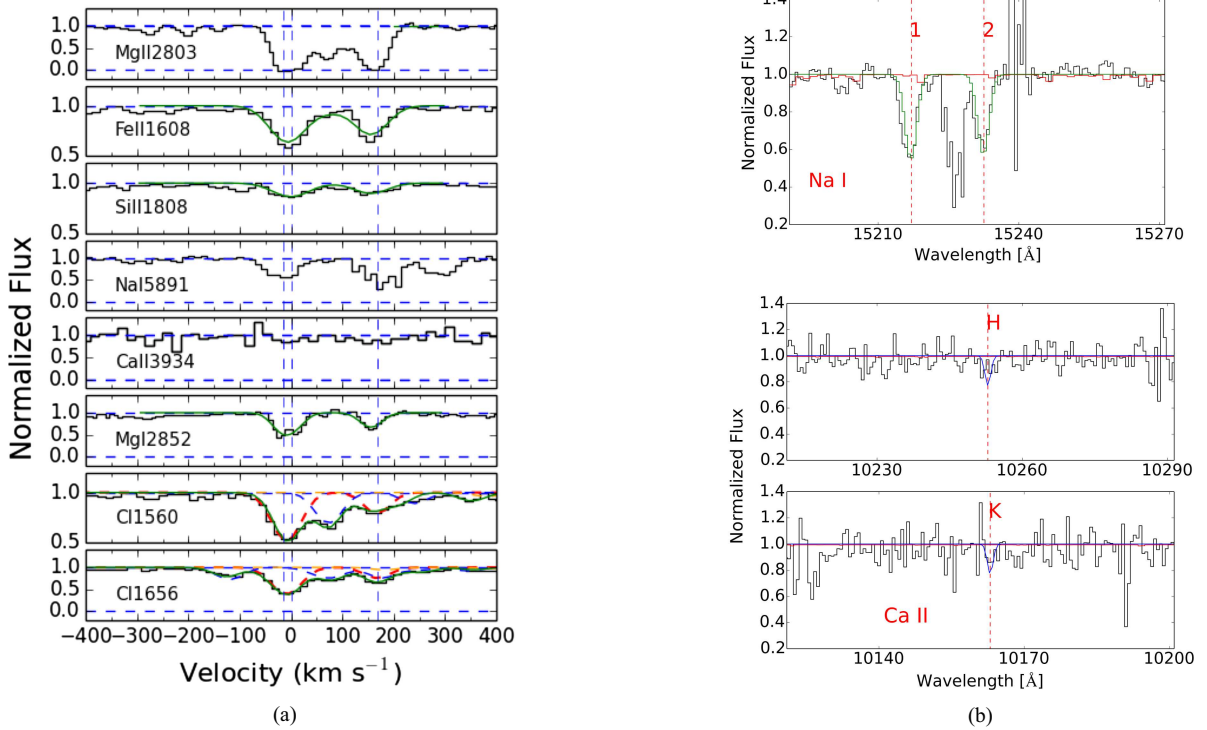
Fig. A.11. J1314+0543: There is a clear detection of Na ɪ D in this system. The spectrum is affected by a spike near Na ɪλ5897, thus we fit the Na ɪλ5891 line and show the corresponding Na ɪλ5897 line. The *EW* values in Table 2 are from the VPFIT fit. There is not apparent detection of Ca ɪɪ and we give upper limits on *EW*. There are two strong components at $v = 0, 160 \, \mathrm{km \, s^{-1}}$ in the Fe ɪɪ, Si ɪɪ, C ɪ, and Mg ɪ absorption profiles. The spike in the spectrum could be due at least partly to Na ɪλ5891 in the second component, the corresponding Na ɪλ5897 being affected by a residual from sky subtraction. We detect Zn ɪɪ, Mn ɪɪ and Ni ɪɪ, with depletion factor [Fe/Zn] = -0.95 ± 0.05.

(a)　　　　　　　　　　　　　　　(b)
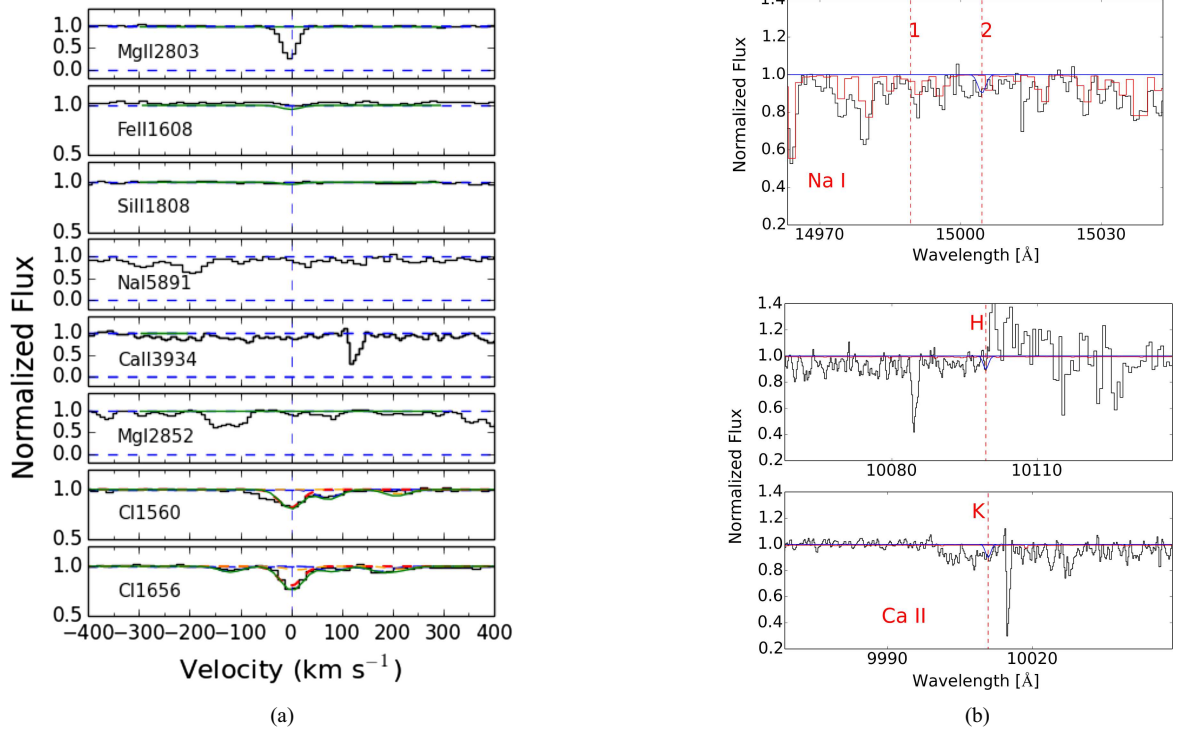
Fig. A.12. J1341+1852: This system is peculiar as it turns out to be a sub-DLA, with column density $\log N(\text{HI}) = 18.18 \pm 0.05$. The C ɪ and other metal line absorptions are weak, with C ɪλ1560 equivalent width $\sim 0.13\,\text{Å}$ (well below the mean $EW = 0.38,\text{Å}$ in the sample), and $W(\text{Mg ɪɪ}\lambda 2798) = 0.33\,\text{Å}$ (for a mean $EW = 2.76\,\text{Å}$ in the sample). The metallicity is high with [OI/HI] = +0.36, relative to solar. It might be interesting to derive the physical properties of this gas and in particular its ionization state. Indeed, it is surprising to detect C ɪ in such a system. This is, however, out of the scope of the present paper. There are no obvious detections of either Ca ɪɪ H&K or Na ɪ D. We give EW upper limits for the lines.


(a)　　　　　　　　　　　　　　　(b)
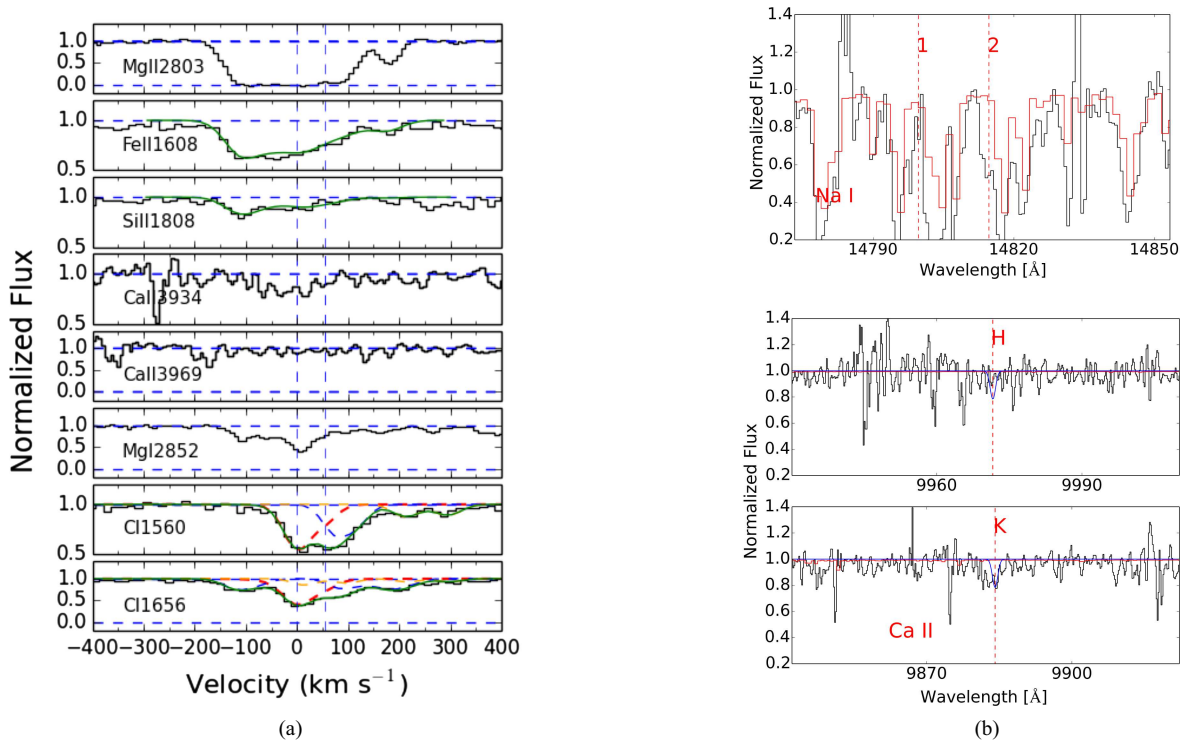
Fig. A.13. J1346+0644: The Na ɪ D line is strongly blended with sky features so that it is difficult to measure even an upper limit. We did not detect Ca ɪɪ i. The C ɪ absorptions are fitted well with two components at $z = 1.511938$ and $z = 1.512393$ ($\Delta v \sim 50\,\text{km s}^{-1}$). The Mg ɪ absorption is extended over $\sim 200\,\text{km s}^{-1}$. The strongest components of Fe ɪɪ and Si ɪɪ are blueshifted by $\sim 100\,\text{km s}^{-1}$ relative to the strongest components of C ɪ and Mg ɪ, which may indicate there is one more component of C ɪ at $-100\,\text{km s}^{-1}$. Since there is basically no flux in the spectrum at wavelengths smaller than 3200 Å, we cannot derive the H ɪ column density.

(a)　　　　　　　　　　　　　(b)
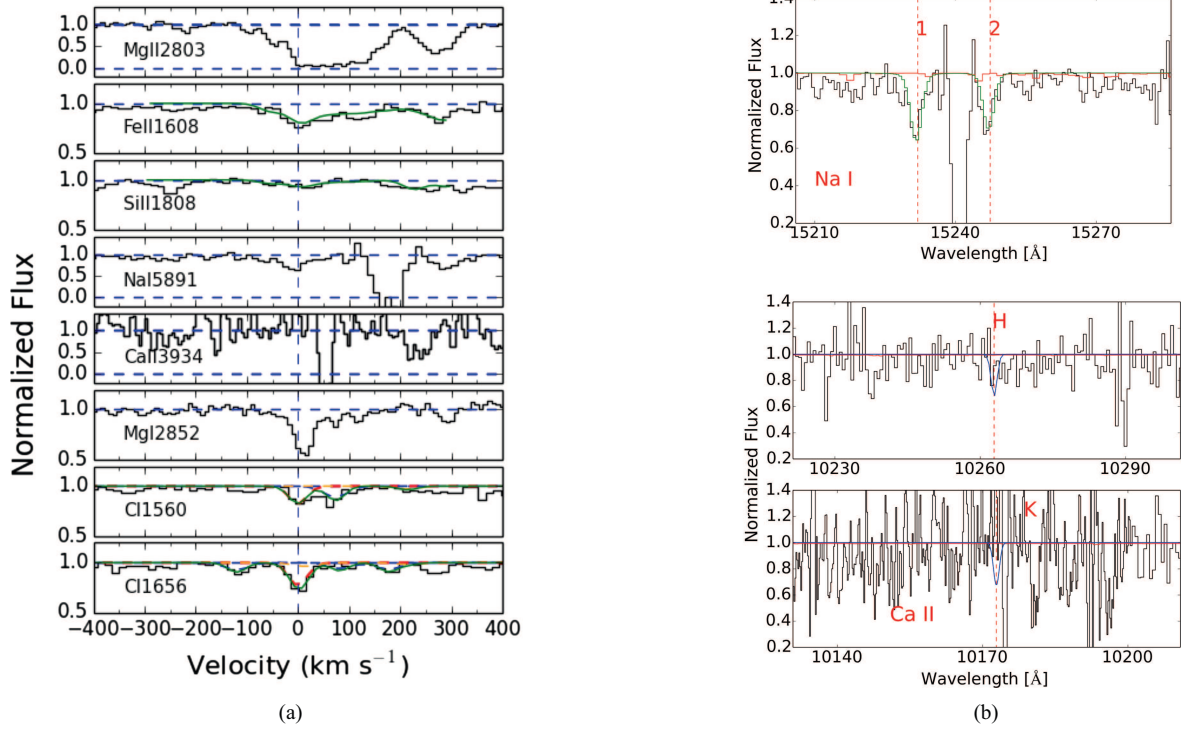
Fig. A.14. J2229+1414: For this system Na ɪ D is clearly detected and strong. We derive upper limits for the Ca ɪɪ lines (0.55 Å). The metal lines are relatively weak compared to other systems. The C ɪ and Mg ɪ main features are located on the blue edge of the Mg ɪɪ profile, which is ~200 km s^{-1} wide.

(a)　　　　　　　　　　　　　(b)
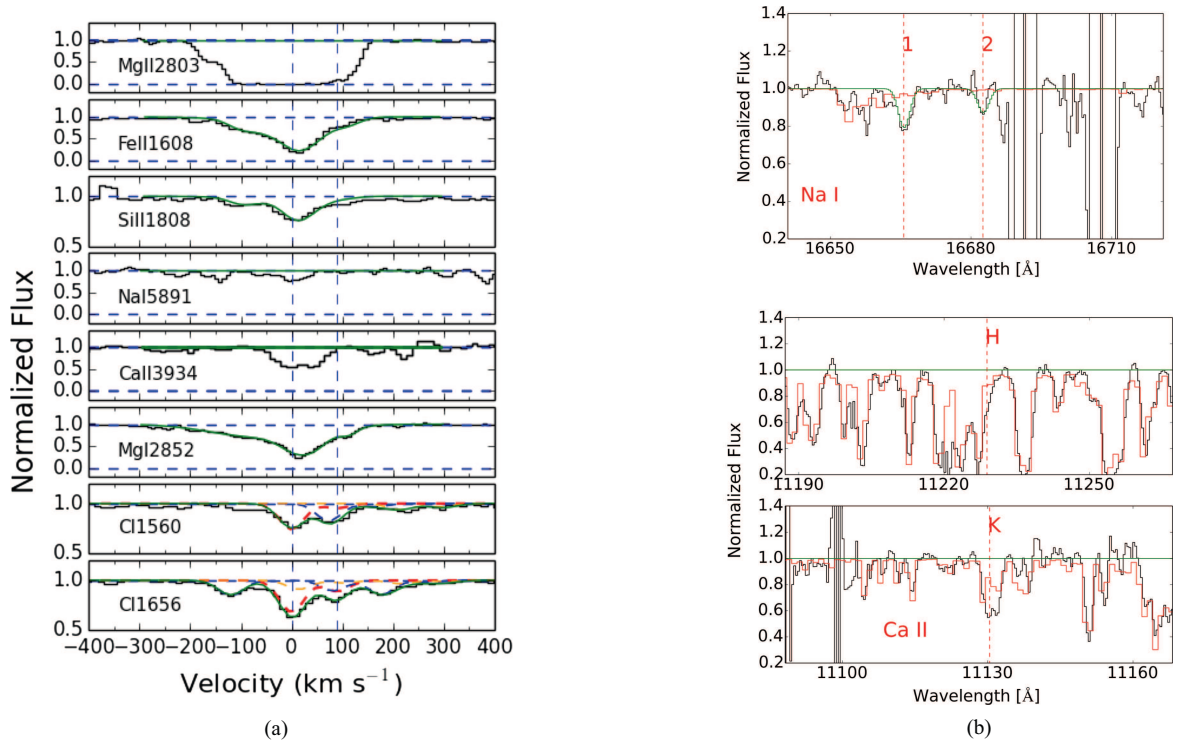
Fig. A.15. J2336−1058: For this system, the Ca ɪɪ doublet is lost in strong sky absorption features. We detect Na ɪ D. The Na ɪλ5891 line is slightly blended with a sky absorption, which is subtracted to derive EW. The C ɪ absorptions are not very strong but we can see two components. The Zn ɪɪ line is detected and we derive a depletion factor [Fe/Zn] = −1.11 ± 0.10.

(a)

(b)
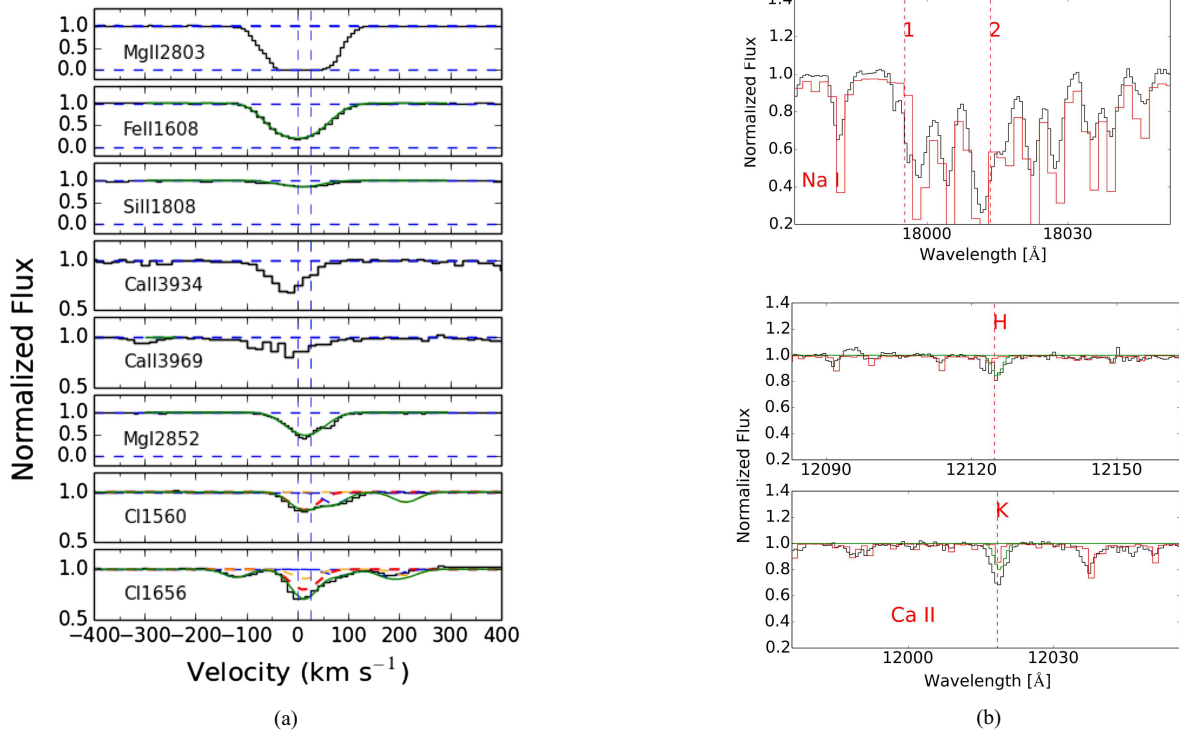
Fig. A.16. J2340−0053: For this system Na I D is lost in telluric absorptions. The C I structure is simple with two components. The Ca II doublet is detected although it is blended with weak sky features. We subtracted the latter. H2 is detected in this system. It is mentioned in Boissé et al. (2015), Balashev et al. (2015), who derived a column density of log $N(H_2) = 18.07 \pm 0.06$.

(a)

(b)
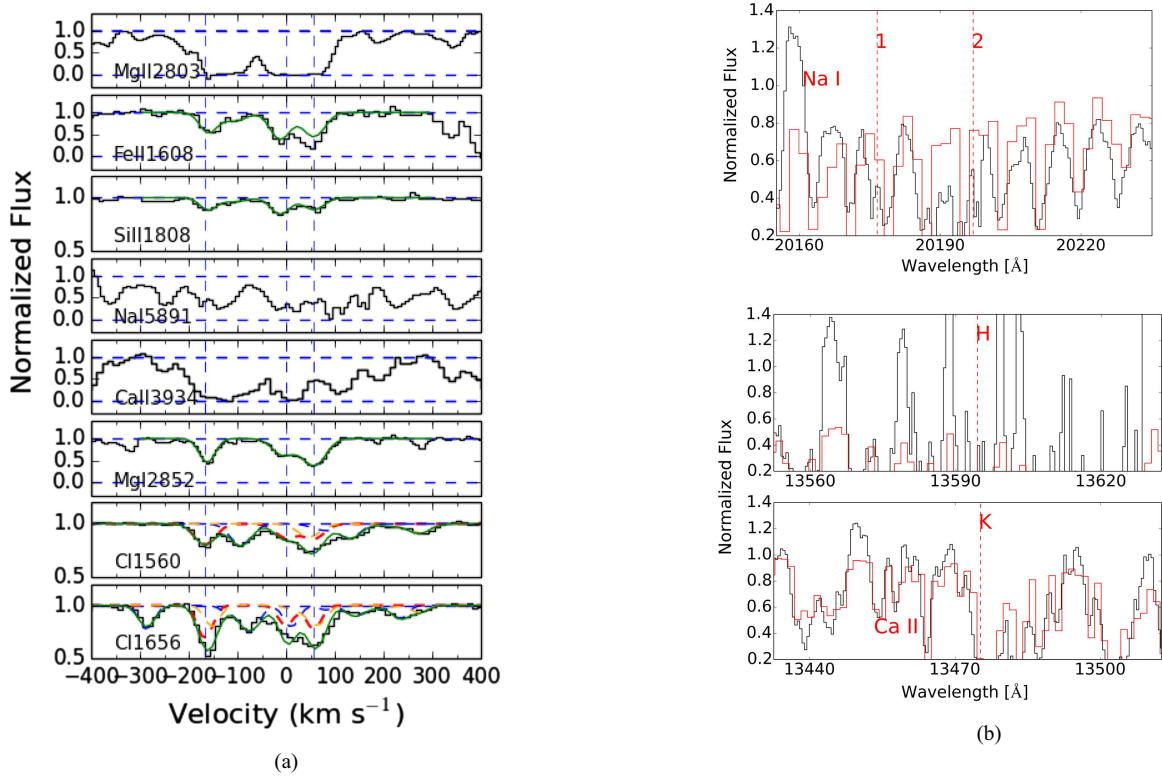
Fig. A.17. J2350−0052: Unfortunately both Na I D and Ca II H&K are lost in telluric absorption features. The Fe IIλ1608 and Fe IIλ1611 lines seem to be blended with other lines. There is a ~ 0.4 Å shift between the UVB and VIS arms that we corrected manually.

Appendix B: E(B − V)
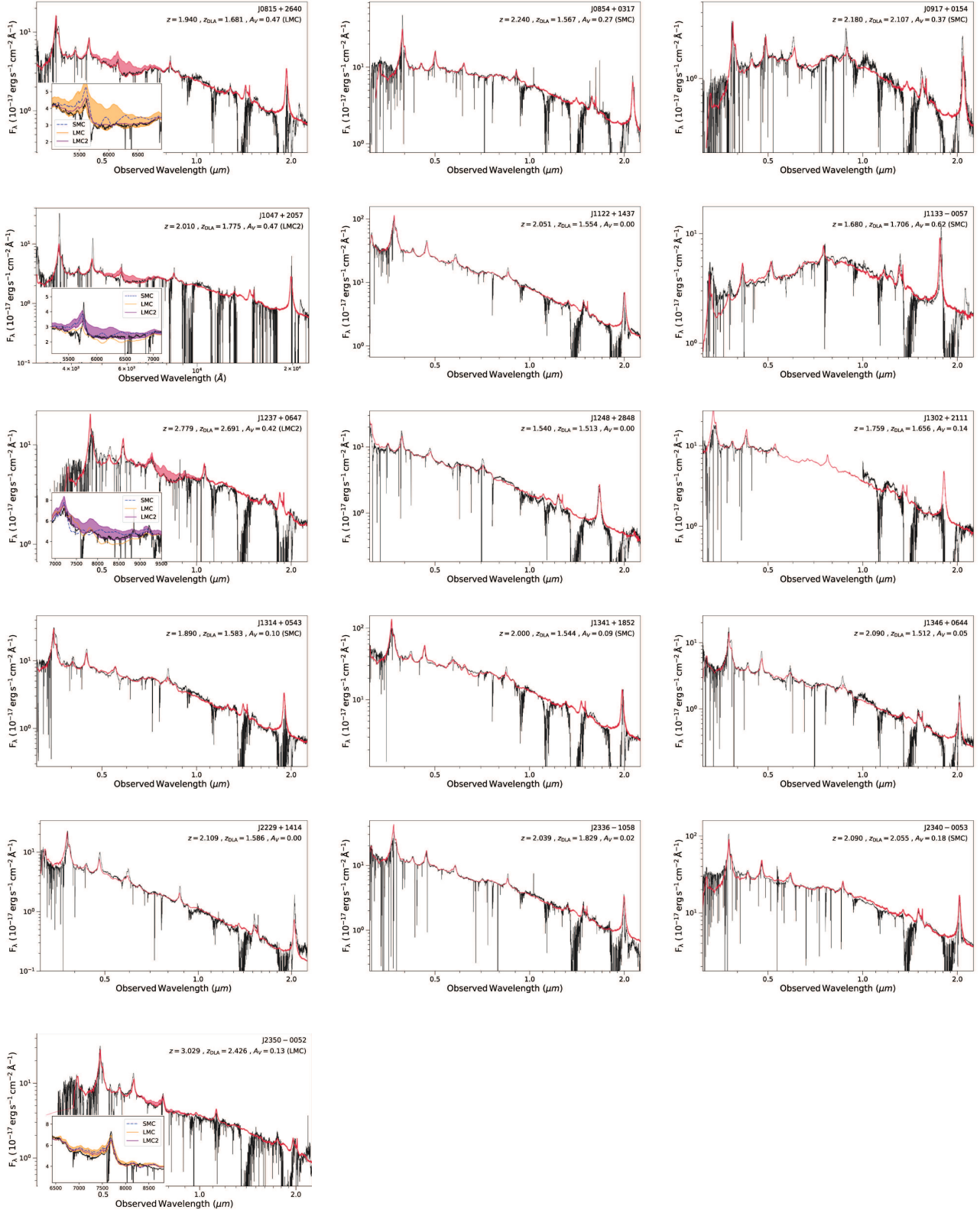
Fig. B.1. X-shooter spectra of quasars in our sample. The red curve corresponds to the quasar template of Selsing et al. (2016) reddened by different extinction curves. See Table 3 for results.